

Chiral Effective Field Theory and the High-Density Nuclear Equation of State

C. Drischler,^{1,2,3} J.W. Holt,⁴ and
C. Wellenhofer,^{5,6}

¹Department of Physics, University of California, Berkeley, California 94720, USA

²Nuclear Science Division, Lawrence Berkeley National Laboratory, Berkeley, California 94720, USA

³Facility for Rare Isotope Beams, Michigan State University, Michigan 48824, USA; email: drischler@frib.msu.edu

⁴Cyclotron Institute and Department of Physics and Astronomy, Texas A&M University, College Station, Texas 77843, USA; email: holt@physics.tamu.edu

⁵Institut für Kernphysik, Technische Universität Darmstadt, 64289 Darmstadt, Germany; email: wellenhofer@theorie.ikp.physik.tu-darmstadt.de

⁶ExtreMe Matter Institute EMMI, GSI Helmholtzzentrum für Schwerionenforschung GmbH, 64291 Darmstadt, Germany

Annu. Rev. Nucl. Part. Sci. 2021. 71:1–31

This article's doi:
10.1146/annurev-nucl-102419-041903

Copyright © 2021 by Annual Reviews.
All rights reserved

Annu. Rev. Nucl. Part. Sci. in press.

Keywords

chiral effective field theory, nuclear matter, neutron stars, many-body perturbation theory, Bayesian uncertainty quantification

Abstract

Born in the aftermath of core collapse supernovae, neutron stars contain matter under extraordinary conditions of density and temperature that are difficult to reproduce in the laboratory. In recent years, neutron star observations have begun to yield novel insights into the nature of strongly interacting matter in the high-density regime where current theoretical models are challenged. At the same time, chiral effective field theory has developed into a powerful framework to study nuclear matter properties with quantified uncertainties in the moderate-density regime for modeling neutron stars. In this article, we review recent developments in chiral effective field theory and focus on many-body perturbation theory as a computationally efficient tool for calculating the properties of hot and dense nuclear matter. We also demonstrate how effective field theory enables statistically meaningful comparisons between nuclear theory predictions, nuclear experiments, and observational constraints on the nuclear equation of state.

Contents

1. Introduction	2
2. From microscopic interactions to the nuclear equation of state	3
2.1. Chiral effective field theory for nuclear forces	3
2.2. Perturbative chiral nuclear interactions	5
2.3. Many-body perturbation theory at zero and finite temperature	7
2.4. Other many-body methods	9
2.5. Implementing three-body forces	10
3. Nuclear equation of state at zero and finite temperature	11
3.1. Confronting nuclear forces with empirical constraints	12
3.2. Nuclear symmetry energy and the isospin-asymmetry expansion	15
3.3. Nuclear thermodynamics	18
4. Applications to neutron star physics	20
4.1. Scales in hot and dense stellar matter	20
4.2. Neutron star structure	20
4.3. Neutron star mergers	23
4.4. Core-collapse supernovae	25
5. Summary and outlook	26

1. Introduction

Neutron stars are one of Nature’s most intriguing astronomical objects and provide a unique laboratory for studying strongly interacting, neutron-rich matter under extreme conditions. With masses of about 1 – 2 times that of the Sun and radii of only approximately 10 km, neutron stars contain the densest form of matter in the observable Universe and lie just at the threshold for collapse to a black hole. Much has already been learned about neutron stars through mass and radius measurements, pulsar timing, x-ray observations, and gravitational-wave measurements of binary mergers in the new era of multimessenger astronomy (see, *e.g.*, Refs. (1, 2, 3) for reviews). But many interesting questions remain to be answered, especially regarding the nature of ultra-compressed matter located in the inner cores of heavy neutron stars where a variety of exotic new states of matter have been theorized to exist.

While neutron stars are bound together by gravity acting over macroscopic length scales, strong short-ranged nuclear interactions provide the essential pressure support to counteract gravitational collapse. The central densities in the heaviest neutron stars may reach up to $5-10 n_0$, where $n_0 \approx 0.16 \text{ fm}^{-3}$ is the nucleon number density typical of heavy atomic nuclei (the associated mass density is $\rho_0 \approx 2.7 \times 10^{14} \text{ g cm}^{-3}$). Although the strong interaction is in principle described by quantum chromodynamics (QCD) over all relevant energy scales, at present no systematic computational method is available to calculate the properties of the high-density matter in the inner cores of heavy neutron stars.

With chiral effective field theory (ChEFT), however, a powerful tool has emerged to carry out microscopic calculations of nuclear matter properties at densities up to around $2n_0$. Instead of QCD’s quarks and gluons, ChEFT is formulated in terms of nucleons and pions (and delta isobars), which are the effective strong interaction degrees of freedom present throughout most of the neutron star interior. In its range of validity, ChEFT provides a systematic expansion for two- and multi-nucleon interactions consistent with the

QCD: quantum chromodynamics

ChEFT: chiral effective field theory

symmetries of low-energy QCD. The unresolved short-distance physics is parameterized in terms of contact interactions whose low-energy couplings are fitted to experimental data. An essential advantage over phenomenological approaches is that theoretical uncertainties can be quantified by analyzing the order-by-order convergence of the ChEFT expansion. In the last few years, the combination of systematic nuclear matter predictions from ChEFT, uncertainty quantification, and neutron star observations has developed into a new avenue for constraining the high-density regime of the nuclear equation of state (EOS).

In this review our aim is to describe recent advances in microscopic ChEFT calculations of the nuclear EOS and their application to neutron stars. [For recent reviews of nuclear structure calculations with ChEFT see, *e.g.*, Refs. (4, 5, 6, 7).] We highlight many-body perturbation theory (MBPT) as an efficient framework for nuclear matter calculations at zero and finite temperature based on chiral two- and multi-nucleon interactions. We also discuss Bayesian methods for quantifying and propagating statistically meaningful theoretical uncertainties. Together with nuclear experiments, astrophysical simulations, and neutron star observations, next-generation ChEFT calculations will be crucial to infer the nature of the extreme matter hidden deep beneath the surface of neutron stars.

The review is organized as follows. In Section 2 we focus on recent progress in deriving nuclear forces from ChEFT and renormalization group (RG) methods to improve the many-body convergence in nuclear matter calculations. We then dedicate Section 3 to recent high-order MBPT calculations of the moderate-density nuclear EOS at zero temperature and advances in the Bayesian quantification of EFT truncation errors. We also discuss finite-temperature calculations and nuclear thermodynamics. In Section 4 we review the present status of the high-density nuclear EOS constrained by nuclear theory, experiment, and observation in the era of multimessenger astronomy, emphasizing the importance of ChEFT. Section 5 ends the review with our summary and perspectives on future advances in nuclear matter calculations and their applications to astrophysics.

EOS: equation of state

MBPT: many-body perturbation theory

RG: renormalization group

2. From microscopic interactions to the nuclear equation of state

In this section, we briefly review delta-less ChEFT and the construction of chiral nuclear interactions as microscopic input for many-body calculations. Applying RG methods allows one to systematically generate (perturbative) low-momentum interactions, for which the nuclear EOS and related observables can be efficiently calculated using MBPT. We discuss both zero- and finite-temperature MBPT, complementary many-body approaches, and the implementation of 3N interactions in nuclear matter calculations.

2.1. Chiral effective field theory for nuclear forces

The interactions among nucleons arise as an effective low-energy phenomenon of QCD, the theory of the strong interaction. At the momentum scales relevant for nuclear physics, $p \sim m_\pi$, QCD is strongly coupled and features nonperturbative effects such as spontaneous chiral symmetry breaking and the confinement of quarks and gluons into hadrons. Direct applications of QCD to hadronic physics at finite density, where lattice QCD faces a formidable sign problem, are therefore extremely challenging and not feasible at present and in the near future. However, one can construct a systematic description of nuclear physics in terms of the effective degrees of freedom at low energies: nucleons and pions (and delta isobars). This effective description is given by ChEFT (8, 9, 10, 11, 12).

The starting point of ChEFT is to write down the most general Lagrangian consistent with the symmetries of low-energy QCD, in particular, the spontaneously broken chiral symmetry, for which pions are the (pseudo) Nambu-Goldstone bosons. This naturally sets a limit for the applicability of ChEFT, *i.e.*, the breakdown scale Λ_b will be of order of the chiral symmetry breaking scale $\Lambda_\chi \sim 1$ GeV. [A Bayesian analysis of free-space NN scattering with several (not-too-soft) chiral NN potentials in Weinberg power counting estimated $\Lambda_b \approx 600$ MeV (13).] A truncation scheme, known as power counting, is then needed to organize the infinite number of operators in the effective Lagrangian in a systematic expansion. This expansion is governed by the *separation of scales* inherent in ChEFT, *i.e.*, the power counting is based on powers of a typical momentum p (or the pion mass) over the ChEFT breakdown scale, $Q = \max(p, m_\pi)/\Lambda_b$.

In perturbative EFT, both power counting and ultraviolet renormalization are essentially unambiguous and straightforward. The situation is different for applications of ChEFT in nuclear physics, where the calculational framework must be able to account for nonperturbative effects such as bound states (atomic nuclei) and large S -wave scattering lengths in NN scattering. While there has been some controversy in the literature as to how the ChEFT expansion should be set up precisely (see, *e.g.*, Refs. (10, 12) and references therein), the prevalent and most successful power counting for ChEFT (in particular regarding many-body applications) is the one first suggested by Weinberg (14, 15, 16)

Within Weinberg power counting, chiral nuclear interactions (and currents) are organized according to naive (*i.e.*, perturbative) dimensional analysis. The nuclear potentials constructed at a given truncation order in the ChEFT expansion are then used for computing observables. Renormalization in this approach is approximative, and carried out by equipping the potentials with regulator functions that suppress contributions above a cutoff scale $\Lambda \lesssim \Lambda_b$, typically chosen in the range 450 – 600 MeV. That is, the cutoff independence of the observables will be achieved only approximatively through Λ -dependent low-energy constants (LECs), which are in practice optimized for a given Λ to reproduce low-energy NN scattering data and few-nucleon observables; see, *e.g.*, Refs. (12, 17). The residual cutoff dependence can then be attributed to higher-order terms in the expansion, so results are expected to become less cutoff dependent with increasing truncation order.

Figure 1 depicts the hierarchy of nuclear interactions up to fifth order (or N^4 LO) in the chiral expansion without delta isobars. [For recent work on the currently less developed delta-full ChEFT, see, *e.g.*, Refs. (18, 19).] In this review, N^k LO indicates (next-to) k -leading order, where k is the number of orders beyond leading order (LO). At each order the interactions are composed of short-range contact interactions as well as one- and multi-pion exchanges at long- and intermediate distances, respectively. The LECs associated with pion exchanges have recently been determined with high precision through an analysis of pion-nucleon scattering within the framework of Roy-Steiner equations (20). The short-range LECs corresponding to NN couplings are generally fixed by matching to NN scattering data. Figure 1 shows that ChEFT naturally predicts the observed hierarchy of two- and multi-nucleon interactions, *i.e.*, $V_{NN} > V_{3N} > V_{4N}$, etc. The first nonvanishing 3N forces appear at N^2 LO in three topologies; from left to right: the long-range two-pion exchange (involving the pion-nucleon LECs c_1 , c_3 , and c_4), intermediate-range one-pion exchange-contact ($\propto c_D$), and short-range 3N contact interaction ($\propto c_E$). At N^3 LO the 3N forces are significantly more involved and operator-rich, and also 4N interactions start to contribute. Apart from the two N^2 LO 3N LECs, c_D and c_E , chiral interactions up to N^3 LO are completely determined by the π N and NN system. While N^4 LO NN forces have already been worked out, partly

NN: nucleon-nucleon

3N: three-nucleon

4N: four-nucleon

LEC: low-energy constant

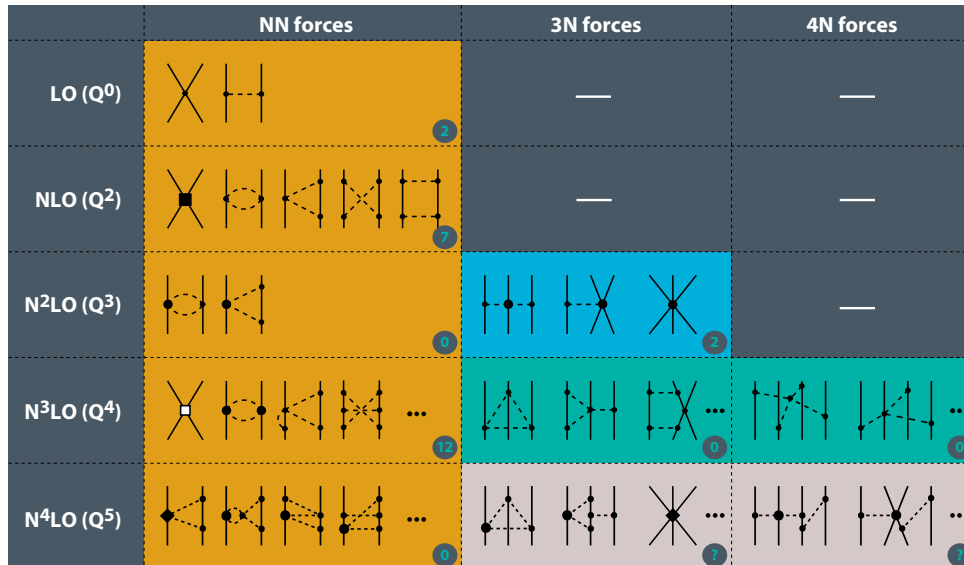


Figure 1: Hierarchy of chiral nuclear interactions up to fifth order (or N⁴LO) in the chiral expansion without delta isobars (12). Nucleons (pions) are depicted by solid (dashed) lines. The circled numbers give the number of short-range contact LECs.

even at N⁵LO, the derivation of N⁴LO 3N interactions has not been finished yet. The 3N LECs c_D and c_E can be fit to (uncorrelated) few-body observables; for instance, the ³H binding energy combined with, *e.g.*, the charge radius of ⁴He, the ³H β -decay half-life, or the nucleon-deuteron scattering cross section. Also heavier nuclei and even saturation properties in infinite nuclear matter have been used to constrain 3N forces.

Although the residual regulator and cutoff dependence of observables at a given chiral order is expected to decrease at higher orders, actual calculations show significant influence of these so-called regulator artifacts on the ChEFT convergence depending on the specific regularization scheme and computational framework. These issues have resulted in the development of a flurry of chiral potentials with nonlocal, local as well as semilocal regulators for a range of cutoff values; see, *e.g.*, Table I of Ref. (21). Moreover, as discussed in Section 2.2, RG methods allow one to modify a given set of two- and multi-nucleon potentials such that observables are left invariant (up to RG truncations) but the convergence of many-body calculations is optimized. These RG transformations are most suitably formulated at the operator (*i.e.*, Hamiltonian) level. The nuclear Hamiltonian constructed at a given order in the ChEFT expansion reads $H = T_{\text{kin}} + V_{\text{NN}}(\Lambda, c_i) + V_{\text{3N}}(\Lambda, c_i) + V_{\text{4N}}(\Lambda, c_i) + \dots$, where Λ stands for the (initial) cutoff or resolution scale, and c_i for the set of LECs inferred from fits to experimental data. The nuclear Hamiltonian is not an observable, and the basic idea of the RG is to exploit this feature to generate more perturbative Hamiltonians.

2.2. Perturbative chiral nuclear interactions

The strong short-range repulsion (“hard core”) and tensor force found in nuclear potentials constructed at cutoff scales $\Lambda \gtrsim 500$ MeV raise questions regarding the applicability of

N^kLO:
(next-to)^k-leading
order

SRG: similarity renormalization group

perturbation theory for many-body calculations. In fact, nuclear many-body calculations were historically considered a nonperturbative problem (see also Section 2.3). Both features give rise to strong couplings between high- and low-momentum states, *i.e.*, large off-diagonal matrix elements, which enhance the intermediate-state summations in perturbation theory. RG methods allow one to amend this feature while preserving nonperturbative few-body results.

The initial application (22) of RG methods to study the scale dependence of nuclear forces was based on T -matrix equivalence, but in recent years the similarity renormalization group (SRG) has been the standard RG method for “softening” nuclear interactions. The SRG decouples high- and low-momentum states through continuous infinitesimal unitary transformations, $H_s = U_s H U_s^\dagger$, described by a differential flow equation in the evolution parameter s . As the SRG flow progresses, the matrix-elements of the NN potential are driven toward a band-diagonal (or block-diagonal) form in momentum space, see Ref. (23) for illustrations. While NN observables are by construction invariant under any RG evolution of the NN potential, A -body observables will remain so only if one also consistently evolves the multi-nucleon part of the nuclear Hamiltonian. The SRG allows one to implement this in principle exactly, in terms of so-called “induced” many-body forces. However, for practical applications, a truncation of the consistent evolution of multi-nucleon interactions is required, *e.g.*, at the 3N level. Neutron matter calculations with SRG-evolved chiral interactions truncated at the 3N level indicate that induced 4N forces are (in that case) negligible within uncertainties for a wide range of SRG resolution scales (24, 25).

There have been many developments recently in the application of ChEFT and SRG technology for the construction of high-precision nuclear potentials. Hebeler *et al.* (26) explored a set of low-momentum N^3 LO NN potentials combined with unevaluated N^2 LO 3N forces where the two 3N LECs were fit to reproduce few-body data (assuming that the 3N contact interactions capture dominant contributions from induced 3N forces). For the softest of these potentials (with $\lambda = 1.8$ and $\Lambda_{3N} = 2.0 \text{ fm}^{-1}$), which was found to predict nuclear saturation properties (26, 27) and ground-state energies of light- to medium-mass nuclei in agreement with experiment (28), Stroberg *et al.* (29) have computed ground-state and separation energies of nearly 700 isotopes up to iron. Moreover, H uther *et al.* (30) have constructed a family of SRG-evolved NN and 3N potentials up to N^3 LO. Also, Reinert *et al.* (17) have developed the first chiral NN potentials up to N^4 LO with semilocal regulators in momentum space such that the long-range part of the pion exchanges remains invariant in contrast to nonlocal regulators. They showed that several N^3 LO contact terms present in previous generations of chiral NN potentials can be eliminated using unitary transformations, leading to considerably softer potentials (even without SRG evolution).

The Weinberg eigenvalue analysis (31, 21) is a powerful tool for quantifying and monitoring the perturbativeness of nuclear forces at different resolution scales. Given an NN potential, the Weinberg eigenvalues $\eta_\nu(W)$ of the operator $G_0(W)V_{NN}$ determine the (rate of) convergence of the Born series for NN scattering. Here, $G_0(W)$ is the (free-space or in-medium) propagator as a function of the complex energy W . The Born series converges if and only if all eigenvalues satisfy $|\eta_\nu(W)| < 1$. Bound states of the potential (such as the deuteron) correspond to $\eta_\nu(W) = 1$ at energies $W < 0$, so the free-space Born series diverges even for soft potentials. In nuclear matter at sufficiently high densities, however, Pauli blocking suppresses the (in-medium) eigenvalues associated with bound (or nearly-bound) states. For potentials constructed at $\Lambda \lesssim 550 \text{ MeV}$, other sources of nonperturbative behavior (such as the hard core) are suppressed as well, both in free-space and in-medium

(see, *e.g.*, Ref. (23) for details). This implies that a nonperturbative treatment of in-medium NN scattering in the particle-particle channel (see Section 2.3) is not mandatory for these interactions. Instead, order-by-order MBPT calculations can be used for systematically studying the many-body convergence of (low-momentum) chiral nuclear interactions.

2.3. Many-body perturbation theory at zero and finite temperature

MBPT starts with partitioning the nuclear Hamiltonian H into a reference one-body part $H_0 = T_{\text{kin}} + U$ and a perturbation $H_1 = V - U$, where T_{kin} is the kinetic-energy operator and U is an effective single-particle potential. We consider here NN-only potentials and discuss the implementation of 3N interactions in Section 2.5. The standard choice for U is the Hartree-Fock potential¹ given by $U_i^{(\text{HF})} = \sum_j V^{ij,ij} f_j$, with the antisymmetrized NN matrix elements $V^{ij,ab} = \langle \mathbf{k}_i \mathbf{k}_j | (1 - P_{12}) V_{\text{NN}} | \mathbf{k}_a \mathbf{k}_b \rangle$, the Pauli exchange operator P_{12} , the momentum integral $\sum_j = \int d^3 k_j / (2\pi)^3$, and the zero-temperature distribution function $f_j = \theta(k_{\text{F}} - k_j)$. For simplicity, we assume here a single-species system and neglect spin-isospin degrees of freedom. In zero-temperature MBPT, the ground-state energy density \mathcal{E} is obtained by expanding H_{int} about its reference value \mathcal{E}_0 . Truncating the many-body expansion at a finite order L then leads to the approximation $\mathcal{E}(k_{\text{F}}) \simeq \mathcal{E}_0(k_{\text{F}}) + \sum_{l=1}^L \mathcal{E}_l(k_{\text{F}})$,² where the Fermi momentum k_{F} is in one-to-one correspondence with the particle number density via $n(k_{\text{F}}) = \sum_i f_i(k_{\text{F}})$.

The first-order correction is determined by the expectation value of $U_i^{(\text{HF})}$ (32). At higher orders it is useful to represent the contributions diagrammatically, *e.g.*, as Hugenholtz diagrams. The diagram and expression for the second-order contribution \mathcal{E}_2 are given by

$$\mathcal{E}_2(k_{\text{F}}) = \begin{array}{c} \text{Diagram: A loop with two vertices. The top vertex has two incoming lines (left and right) and two outgoing lines (left and right). The bottom vertex has two incoming lines (left and right) and two outgoing lines (left and right). A horizontal line connects the two vertices, crossing the vertical lines. Arrows on the vertical lines indicate the direction of flow: upwards on the left and downwards on the right. \end{array} = -\frac{1}{4} \sum_{ijab} V^{ij,ab} V^{ab,ij} f_{ij} \bar{f}_{ab} \frac{1}{D_{ab,ij}}, \quad (1)$$

with the distribution functions $f_{ij} = f_i f_j$ (holes) and $\bar{f}_{ab} = (1 - f_a)(1 - f_b)$ (particles), energy denominator $D_{ab,ij} = \varepsilon_a + \varepsilon_b - \varepsilon_i - \varepsilon_j$, and single-particle energies $\varepsilon_i = k_i^2 / (2M) + U_i^{(\text{HF})}$. Writing down the expression associated with a diagram follows these simple rules:

- Each vertex gives a factor $V^{ij,ab}$, with i and j are the lines directed toward the vertex, and a and b are the lines directed away from the vertex.
- Downwards lines give factors of f_i while upwards lines give $(1 - f_i)$, corresponding to hole and particle excitations of the reference ground-state, respectively, and
- For adjacent vertices there is an energy denominator given by subtracting the energy of the reference ground-state from the excited state corresponding to the particle and hole lines that are crossed by a virtual horizontal line between the two vertices.

Each diagram's overall factor can be inferred from the diagrammatic structure as well (32). For instance, the expression of the third-order particle-particle (pp) diagram reads

$$\mathcal{E}_{3,pp}(k_{\text{F}}) = \begin{array}{c} \text{Diagram: A loop with three vertices. The top vertex has two incoming lines (left and right) and two outgoing lines (left and right). The bottom-left vertex has two incoming lines (left and right) and two outgoing lines (left and right). The bottom-right vertex has two incoming lines (left and right) and two outgoing lines (left and right). A horizontal line connects the two bottom vertices, crossing the vertical lines. Arrows on the vertical lines indicate the direction of flow: upwards on the left and downwards on the right. \end{array} = \frac{1}{8} \sum_{ijabcd} V^{ij,ab} V^{ab,cd} V^{cd,ij} f_{ij} \bar{f}_{abcd} \frac{1}{D_{ab,ij} D_{cd,ij}}. \quad (2)$$

¹In Hartree-Fock MBPT, the $-U$ part of $H_1 = V - U$ cancels all diagrams involving single-vertex loops (32, 27, 25).

²The many-body expansion is in fact a divergent asymptotic series, but the divergent behavior is expected to appear only for high truncation orders $L \gtrsim 20$ (33).

Finding all valid diagrams (and associated expressions) at a given MBPT order has been formalized using graph-theory methods (34): in Hartree-Fock MBPT there are (1, 3, 39, 840, 27300) diagrams at order $l = (2, 3, 4, 5, 6)$. Together with the automated code generation for the efficient Monte Carlo integration of arbitrary MBPT diagrams developed in Ref. (27), this has led to a fully automated approach to MBPT calculations.

In the traditional Brueckner (or G -matrix) approach (35), the pp ladder diagrams are resummed to all orders, motivated by the large high-momentum components of traditional NN potentials to which the pp ladders are particularly sensitive. The pp bubbles in these diagrams are even ultraviolet divergent if the potential is not sufficiently suppressed at high momenta. For modern low-momentum potentials, however, the pp ladders no longer play a distinguished role in the many-body expansion, and explicit MBPT calculations at third and fourth order have shown that they are not enhanced compared to other diagrams at the same order (27). Nevertheless, partial diagrammatic resummations are still pertinent for consistent calculations of in-medium single-particle properties and response functions as performed in the self-consistent Green's functions method (for more details see Section 2.4).

The consistent generalization of MBPT to finite temperatures ($T > 0$) is a nontrivial issue. From the standard finite- T perturbation series for the grand-canonical potential³

$$\Omega(T, \mu) \simeq \Omega_0(T, \mu) + \sum_{l=1}^L \Omega_l(T, \mu), \quad (3)$$

the free energy density $\mathcal{F}(T, \mu)$ is obtained via the thermodynamic relation $\mathcal{F}(T, \mu) = \Omega(T, \mu) + \mu n(T, \mu)$. Here, the density is given by $n(T, \mu) = -\partial\Omega(T, \mu)/\partial\mu$. The issue is now that the relations between (\mathcal{F}, n) and (\mathcal{E}, n) obtained in finite- and zero- T MBPT, respectively, do not match in the limit $T \rightarrow 0$ (as discussed further below).

Regarding this, we first consider the finite- T expression for the second-order diagram,

$$\Omega_2(T, \mu) = \begin{array}{c} \bullet \\ \updownarrow \\ \bullet \end{array} = -\frac{1}{4} \sum_{ijab} V^{ij,ab} V^{ab,ij} f_{ij} \bar{f}_{ab} \mathcal{G}_2. \quad (4)$$

Equation (4) differs only slightly from $\mathcal{E}_2(k_F)$ in Eq. (1). First, the energy denominator is replaced by $\mathcal{G}_2 = (1 - e^{-D_{ab,ij}/T})/(2D_{ab,ij})$. The numerator in this expression vanishes at any zero of the denominator, *i.e.*, there are no poles at finite T . In the $T \rightarrow 0$ limit the integration regions corresponding to the two terms in the numerator of \mathcal{G}_2 separate into two equivalent parts (with integrable poles at the integral boundaries), *i.e.*, $\mathcal{G}_2 \rightarrow 1/D_{ab,ij}$ for $T \rightarrow 0$. These features pertain for higher-order diagrams (36).⁴ The second difference at finite T compared to $T = 0$ is that the $f_i = f_i(T, \mu)$ are Fermi-Dirac distributions instead of step functions centered at the Fermi energy ε_{k_F} .

Similar to the free Fermi gas (*i.e.*, MBPT with $U = 0$ and $L = 0$), for Hartree-Fock MBPT at $L = 1$, the chemical potential μ at $T = 0$ matches the reference Fermi energy ε_{k_F} , with $n(T, \mu) = \sum_i f_i(T, \mu)$ (36). But these relations cease to be valid at higher orders due to higher-order contributions in the expression for $n(T, \mu)$. Note that these contributions involve factors $\partial f_i/\partial\mu = f_i(1 - f_i)/T$, which become $\delta(\varepsilon_i - \mu)$ at $T = 0$ (so there is a

³Using the grand-canonical ensemble is required for the evaluation of quantum-statistical averages in the thermodynamic limit.

⁴The poles (at the integral boundary) at $T = 0$ lead to nonanalyticities in the asymmetry dependence of the nuclear EOS, see Section 3.2.

nonvanishing contribution at $T = 0$). Contributions involving factors $f_i(1 - f_i)/T$ are also present in certain perturbative contributions to Ω , starting at fourth order for Hartree-Fock MBPT (36). [For $U = 0$, they appear already at second order.] These contributions can be associated with the presence of additional so-called anomalous diagrams in finite- T MBPT, see Refs. (37, 36) for more details. As evident from the discussion above (*i.e.*, below Eq. (4)), the $T \rightarrow 0$ limit of the finite- T expressions for normal (*i.e.*, not anomalous) contributions Ω_l matches the corresponding zero- T contributions \mathcal{E}_l , except that the reference Fermi energy is replaced by the (true) chemical potential. Therefore, a consistent finite- T version of Hartree-Fock MBPT for $L \leq 3$ would be given by

$$\mathcal{F}(T, \tilde{\mu}) \simeq \mathcal{F}_0(T, \tilde{\mu}) + \sum_{l=1}^L \mathcal{F}_l(T, \tilde{\mu}), \quad (5)$$

where $\mathcal{F}_l = \Omega_l$ (for $l = 1, 2, 3$) and the auxiliary “chemical potential” $\tilde{\mu}$ is related to the density via $n(T, \tilde{\mu}) = \sum_i f_i(T, \tilde{\mu})$, implying $\tilde{\mu} \rightarrow \varepsilon_{k_F}$ in the $T \rightarrow 0$ limit.⁵

In the $U = 0$ case, the method for constructing a finite- T perturbation series of the form of Eq. (5) for any L is well known (37): one expands each contribution to $\mathcal{F}(T, \mu)$ about $\tilde{\mu}$ according to $\mu = \tilde{\mu} + \sum_{i=1}^L \mu_i(T, \tilde{\mu})$ while neglecting all terms beyond the truncation order L . [The terms μ_i are determined by the requirement that the truncated expansion of $n(T, \mu)$ about $\tilde{\mu}$ reproduces $n(T, \tilde{\mu}) = \sum_i f_i(T, \tilde{\mu})$.] This process can also be applied to Hartree-Fock MBPT (25), with the caveat that the single-particle potential has to be evaluated at $\tilde{\mu}$, *i.e.*, no derivatives of $U_i^{(\text{HF})}(T, \tilde{\mu})$ in $\tilde{\mu}$ appear. In both cases, $U = 0$ and Hartree-Fock MBPT, the resulting perturbation series for the free energy reproduces zero- T MBPT at each truncation order L , even though the terms \mathcal{F}_l contain anomalous contributions for $l \geq 4$ ($l \geq 2$, for $U = 0$). The fact that Eq. (5) results from a truncated re-expansion shows explicitly that the original grand-canonical series is not consistent with zero- T MBPT. For general arguments why the free-energy series is expected to give improved results compared to grand-canonical MBPT, see Refs. (36, 38).

Altogether, MBPT as formulated in the free-energy series [Eq. (5)] provides a consistent framework for nuclear matter calculations at zero- and finite-temperature, where many-body uncertainties can be systematically assessed by increasing the truncation order L . Although the number of MBPT diagrams increases rapidly with L , the technologies recently developed for automated diagram generation and evaluation (34, 27) enable calculations at high-enough orders to probe in detail the many-body convergence for chiral low-momentum NN and 3N interactions. Furthermore, exploring MBPT with single-particle potentials beyond the Hartree-Fock level is an important task for future research. In particular, the single-particle potential U can be chosen at each truncation order such that the grand-canonical and free-energy series are also equivalent for $L > 1$ (36); for Hartree-Fock MBPT, they are only equivalent for $L = 1$. First investigations of this order-by-order renormalization of the single-particle potential have shown that higher-order contributions to U can have a significant effect on low-order MBPT results and the many-body convergence (39).

2.4. Other many-body methods

The advances in ChEFT and RG methods have established MBPT as a central approach for studying the nuclear EOS at zero and finite temperature. While MBPT is the focus of

⁵The true chemical potential is obtained from $\mathcal{F}(T, \tilde{\mu})$ via $\mu = \partial\mathcal{F}/\partial n$.

this review, various other many-body methods have been applied in initial nuclear matter studies with chiral NN and 3N interactions. In particular, nonperturbative frameworks are important to benchmark the MBPT convergence and probe aspects of many-body physics beyond the nuclear EOS. Below we will briefly discuss the *self-consistent Green's functions (SCGF) approach* and *Quantum Monte Carlo (QMC) methods*. Other methods not discussed here for brevity are coupled-cluster (CC) theory (40), the in-medium SRG (4), and lattice EFT (41). Systematic comparisons between different many-body frameworks will provide a coherent picture of microscopic interactions and nuclear many-body properties.

The SCGF approach (42, 43) is based on the self-consistent computation of in-medium propagators (or Green's functions) in Fourier (Matsubara) space, corresponding to the to-all-orders resummation of some perturbative contributions to the propagators. SCGF calculations of the nuclear EOS at zero and finite temperature (44, 45) have been implemented using the in-medium T -matrix approximation, where the ladder diagrams are resummed to all orders, providing a thermodynamically consistent generalization of Brueckner theory (43). Furthermore, SCGF calculations have been used to benchmark the order-by-order convergence of MBPT (up to third order) in neutron matter (46). The energy per particle obtained in SCGF and MBPT was found to agree well for a range of unevolved chiral NN and 3N interactions up to N^3 LO. The SCGF approach allows for fully consistent computations of response functions and transport properties, which will be vital for comparisons with MBPT calculations of these quantities.

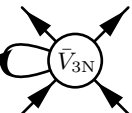
QMC refers to a family of stochastic methods that solve the many-body Schrödinger equation through random sampling (6). As such, QMC methods are truly nonperturbative and provide important benchmarks for many-body methods with basis expansions. However, apart from the fermion sign problem a caveat is that most QMC methods require local nuclear potentials to obtain low-variance results, restricting both the regularization scheme and the interaction operators that can be included in the ChEFT expansion. QMC calculations with local chiral NN and 3N potentials up to N^2 LO have been carried out in neutron matter (47, 48) and recently also symmetric nuclear matter (49). Because of Fierz invariance breaking, the regulator artifacts are significantly larger than in MBPT calculations with nonlocal potentials. On the other hand, since QMC methods are not restricted to soft interactions, a much wider range of momentum cutoffs can be studied with QMC. Hence, QMC methods can provide important insights into the residual cutoff dependence of observables and the breakdown scale of ChEFT at high densities.

2.5. Implementing three-body forces

Three-nucleon forces are crucial for understanding properties of finite nuclei and nuclear matter (7), such as drip lines along isotopic chains and nuclear saturation in SNM. Even though partial-wave decomposed matrix elements of chiral 3N forces have become available recently up to N^3 LO (50), implementing 3N forces in many-body calculations remains computationally difficult and usually requires approximations (51). The large uncertainties due to 3N forces, *e.g.*, in the nuclear EOS at densities $n \gtrsim n_0$, emphasize the need for improving these approximations as well as developing novel chiral NN and 3N potentials in general.

Normal ordering allows one to include dominant 3N contributions in many-body frameworks using density-dependent effective two-body potentials (52). Through Wick's theorem the general three-body Hamiltonian can be *exactly* normal ordered with respect to a finite-density reference state (*e.g.*, the Fermi sea of noninteracting nucleons or the Hartree-Fock

ground state) instead of the free-space vacuum (23). This shifts contributions from the three-body Hamiltonian operator to effective zero-body, one-body, and two-body operators plus a residual (reduced) three-body operator. A many-body framework built for NN interactions can then incorporate a density-dependent effective interaction $V_{\text{NN}}^{\text{med}}$ derived from $V_{3\text{N}}$ as $V_{\text{NN}} \rightarrow V_{\text{NN}} + \xi V_{\text{NN}}^{\text{med}}$. The combinatorial factor ξ is determined by Wick's theorem and depends on the many-body calculation of interest. The matrix elements of $V_{\text{NN}}^{\text{med}}$ are obtained by summing one particle over the occupied states in the reference state:

$$\langle \mathbf{2}'\mathbf{3}' | V_{\text{NN}}^{\text{med}} | \mathbf{2}\mathbf{3} \rangle = \text{Diagram} = \sum_{\sigma_1 \tau_1} \int \frac{d\mathbf{k}_1}{(2\pi)^3} f_1 \langle \mathbf{12}'\mathbf{3}' | \bar{V}_{3\text{N}} | \mathbf{123} \rangle, \quad (6)$$


with the shorthand notation $|\mathbf{i}\rangle = |\mathbf{k}_i \sigma_i \tau_i\rangle$, antisymmetrized 3N interactions $\bar{V}_{3\text{N}}$, and momentum distribution function of the reference state f_1 .

In contrast to the (Galilean-invariant) NN potential, the effective two-body potential (6) depends on the center-of-mass momentum \mathbf{P} of the two remaining particles. Hence, both potentials cannot be straightforwardly combined in a partial-wave basis and different approximations for the \mathbf{P} dependence have been used to enable applications to nuclear matter. Under the assumption that $\mathbf{P} = 0$ first implementations evaluated Eq. (6) semi-analytically in symmetric nuclear matter and pure neutron matter starting from the N²LO 3N interactions (53, 54, 26). Extensions to asymmetric nuclear matter and finite temperature have followed (38, 55, 46, 56), and a new method that allows for the construction of an effective two-body potential from any partial-wave decomposed 3N interaction in an improved \mathbf{P} angle-averaging approximation has been developed (56). The latter approach is especially advantageous for studying 3N forces at N³LO (56), bare and SRG-evolved, and in different regularization schemes. Semi-analytic expressions along the lines of Ref. (53) have been derived up to N³LO and also partially to N⁴LO (57).

The three-body term in the normal-ordered Hamiltonian cannot be implemented using effective two-body potentials. In nuclear matter such residual 3N contributions have been studied in CC (58) and MBPT calculations (59, 60, 61, 27). Explicit calculations of the residual 3N diagram in MBPT at second order,

$$\mathcal{E}_2^{\text{res}}(k_F) = \text{Diagram} = -\frac{1}{36} \sum_{ijkabc} V^{ijk,abc} V^{abc,ijk} f_{ijk} \bar{f}_{abc} \frac{1}{D_{abc,ijk}}, \quad (7)$$


showed for a range of chiral interactions that its contribution is typically much smaller than both the overall EFT truncation error and the individual contributions from the other MBPT diagrams up to this order (27). While these findings give some justification for the commonly used approximation where residual 3N contributions are neglected, the automated approach introduced in Ref. (27) implements chiral NN, 3N, and 4N interactions *exactly* in nuclear matter calculations using a single-particle spin-isospin basis. Combined with high-performance computing, this method sets the stage for systematic studies of ChEFT interactions in MBPT up to high orders without the mentioned approximations.

3. Nuclear equation of state at zero and finite temperature

In this Section we survey recent nuclear matter calculations up to $n \approx 2n_0$ in MBPT with chiral NN and 3N interactions. We discuss advances in the quantification and propagation

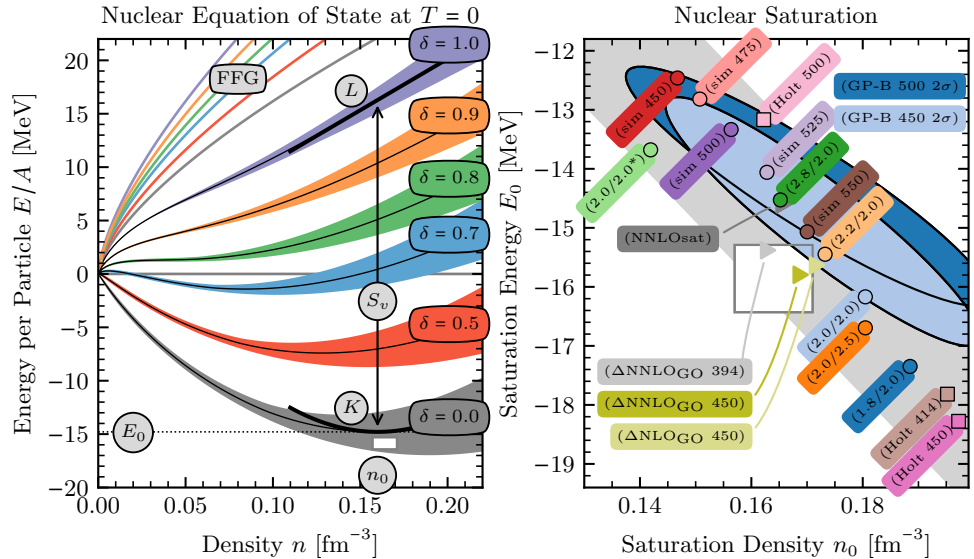


Figure 2: (left) Nuclear EOS at $T = 0$ as a function of density n for a representative set of isospin asymmetries δ . The uncertainty bands in the energy per particle E/A were obtained in Ref. (56) by second-order MBPT calculations based on the Hebeler *et al.* interactions (26). Key observables that characterize $E(n \approx n_0, \delta)/A$ are illustrated: the saturation point (n_0, E_0) , incompressibility K_0 , symmetry energy S_v and its slope parameter L at n_0 . (right) Saturation points of numerous chiral interactions from fourth- (circles) and third-order (squares) MBPT calculations, as well as CC theory (triangles); specifically, the NN and 3N interactions by Hebeler *et al.* (26) (as in (left), “ λ/Λ_{3N} [fm^{-1}]”), Carlsson *et al.* (62) (“sim Λ [MeV]”), and Holt *et al.* (39, 63) (“Holt Λ [MeV]”). The ellipses show the 2σ regions of order-by-order calculations up to $N^3\text{LO}$ in MBPT with EFT truncation errors fully quantified (64). Note that the saturation points are aligned along a Coester-like band (gray anticorrelation band). The white box in each panel depicts the empirical saturation point, $E_0 = -15.86 \pm 0.57$ MeV with $n_0 = 0.164 \pm 0.007$ fm^{-3} (56). The Hamiltonian “2.0/2.0*” uses the c_i values from the NN partial-wave analysis in Ref. (65) in the 3N forces. The data in the right panel were taken from Refs. (18, 27, 39, 64).

of EFT truncation errors, confront different microscopic constraints on the nuclear symmetry energy with experiment, and examine contributions beyond the standard quadratic expansion of the EOS in the isospin asymmetry. We conclude the Section with results for the nuclear liquid-gas phase transition at finite temperature.

3.1. Confronting nuclear forces with empirical constraints

Figure 2 (left) illustrates the nuclear EOS at zero temperature as a function of density n for a representative set of isospin asymmetries $\delta = (n_n - n_p)/n$, where n_n (n_p) is the neutron (proton) number density. Several general observations can be gleaned. Nuclear interactions are much stronger in SNM compared to PNM, which is closer to the free Fermi gas (FFG, solid lines). Consequently, the uncertainties are larger in SNM, especially for densities $n \gtrsim n_0$. In PNM they are well controlled for $n \lesssim n_0$, and a wide range of

chiral NN and 3N interactions lead to similar results for PNM (see, *e.g.*, Refs. (66, 7, 67)). Increasing uncertainties toward higher densities are predominantly due to 3N interactions. Although the complexity of 3N interactions is much reduced in PNM (54), they provide at all values of δ important repulsive contributions that grow stronger with the density than those of NN interactions. The 3N interactions are therefore crucial for understanding the high-density EOS and the structure of neutron stars. In PNM all chiral interactions up to N³LO are completely determined by the π N and NN system. The intermediate- and short-range 3N interactions at N²LO that are proportional to the LECs c_D and c_E , respectively, vanish (for regulators symmetric in the particle labels) due to the coupling of pions to spin and the Pauli principle, respectively. Also the long-range two-pion exchange 3N forces at N²LO are simplified since the LEC c_4 does not contribute. This allows for tight low-density constraints on the neutron-rich matter EOS from PNM calculations and systematic high-density extrapolations (see Section 4).

Nuclear matter represents an ideal system for testing nuclear interactions at the densities accessible to laboratory experiments and their implementation in many-body methods. As illustrated in Fig. 2 (left), the nuclear EOS in the vicinity of n_0 is (to good approximation) characterized by only a few experimentally accessible quantities. That is, the EOS of SNM can be expanded about its minimum n_0 as $E(n, \delta = 0)/A \approx E_0 + (K/2)\eta^2$, with the saturation energy $E_0 = E(n_0, 0)/A$, incompressibility K , and $\eta = (n - n_0)/(3n_0)$. Further, explicit ANM calculations with chiral NN and 3N interactions (56, 68, 69) have shown that the asymmetry dependence of the nuclear EOS is reasonably well reproduced by the standard quadratic approximation $E(n, \delta)/A = E(n, 0)/A + E_{\text{sym}}(n)\delta^2$, where the symmetry energy expanded in density reads $E_{\text{sym}}(n) \approx S_v + L\eta$. In this approximation one finds $E(n, 1)/A \approx (E_0 + S_v) + L\eta$ for PNM. Microscopic predictions and empirical constraints for (n_0, E_0, K) and (S_v, L) can then be confronted with one another.⁶

Nuclear saturation emerges from a delicate cancellation between kinetic and interaction contributions to the EOS. Reproducing empirical constraints on (n_0, E_0, K) is therefore an important benchmark of nuclear interactions, especially 3N forces (providing the necessary repulsion). Figure 2 (right) depicts the saturation points of numerous chiral potentials as predicted by fourth- (circles) and third-order (squares) MBPT calculations. The saturation points are aligned along a Coester-like band (gray anticorrelation band), which overlaps with the empirical saturation point (white boxes, see legend), determined from a set of energy density functionals (71). Also shown are results from CC calculations with NNLO_{sat} (▶) and the new deltaful chiral potentials (18) “ Δ NLO_{GO} Λ [MeV]” and “ Δ NNLO_{GO} Λ [MeV]” (▶, ▶, ▶), constructed by the Gothenburg-Oak-Ridge (GO) collaboration. Only the latter fall into the empirical range for (n_0, E_0) . However, judging the extent a nuclear potential reproduces empirical (saturation) properties can be quite misleading without taking meaningful uncertainties into account; especially, the truncation of the EFT expansion at a finite order can result in sizable EFT truncation errors (even at N³LO) that need to be quantified.

Until a few years ago, the prevalent way of estimating theoretical uncertainties in nuclear matter calculations was parameter variation within some (arbitrary) range; that is, probing the observable’s sensitivity to, *e.g.*, the 3N LECs or momentum cutoff. Recently, the focus has been more on the systematic quantification of EFT truncation errors (72), which can be estimated by assuming that an observable’s EFT convergence pattern at order k

PNM: pure neutron matter ($\delta = 1$)

ANM: asymmetric nuclear matter ($0 < \delta < 1$)

SNM: symmetric nuclear matter ($\delta = 0$)

FFG: free Fermi gas

⁶See Ref. (70) for a review of the link between the nuclear EOS and nuclear observables; *e.g.*, from measurements of the isoscalar giant monopole resonance $K \approx 210 - 230$ MeV was inferred.

takes the form $y_k(n) = y_{\text{ref}}(n) \sum_{m=0}^k c_m(n) Q^m(n)$ (73). Here, $y_{\text{ref}}(n)$ sets a dimensionful reference scale, $Q(n)$ is the dimensionless expansion parameter, and the $c_m(n)$ are the dimensionless coefficients not to be confused with the LECs of the interaction (*e.g.*, $y_4 = E/A$ at N³LO). Note that $c_1 = 0$ in Weinberg power counting. For given choices of $y_{\text{ref}}(n)$ and $Q(n)$,⁷ the $c_{m \leq k}(n)$ are obtained from order-by-order calculations $\{y_0, y_1, \dots, y_k\}$ of the observable. Since $y_{\text{ref}}(n)$ and $Q(n)$ factor in all physical scales, the $c_m(n)$ are expected to be of order one (*i.e.*, *natural*), unless the coefficients are fine-tuned. The standard EFT uncertainty, which assumes that the truncation error is dominated by the first omitted term, has been implemented by Epelbaum *et al.* (74) and applied to a wide range of observables in finite nuclei and infinite matter. This “EKM uncertainty” can be summarized at N^jLO as $\delta y(n) = y_{\text{ref}} Q^{j+2} \max(|c_0|, |c_1|, \dots, |c_{j+1}|)$, whose point-wise estimates can be interpreted as Bayesian credibility regions under a particular choice of priors for c_m (13).

The *Bayesian Uncertainty Quantification: Errors in Your EFT* (BUQEYE) Collaboration has recently introduced a Bayesian framework for quantifying correlated EFT uncertainties in the nuclear EOS (75, 64).⁸ In contrast to the standard EFT uncertainty, the new framework allows for the quantification *and* propagation of statistically meaningful uncertainties to derived quantities (*e.g.*, the pressure) while accounting for correlations across densities and between observables. Without considering these correlations, uncertainties can be overestimated. The framework also includes Bayesian model checking tools (76) for diagnosing and testing whether the in-medium ChEFT expansion works as assumed (*e.g.*, inference for Λ_b). Gaussian Processes (GPs) with physics-based hyperparameters are trained on the order-by-order calculations of the energy per particle under the assumption that all $c_m(n)$ are random curves drawn from a single GP (73). The Gaussian posterior for the $c_m(n)$ is then used to estimate the to-all-orders EFT truncation error $\delta y_k(n) = y_{\text{ref}}(n) \sum_{m=k+1}^{\infty} c_m(n) Q^m(n)$ and combined with additional (*e.g.*, many-body) uncertainties. From the posterior also arbitrary derivatives in n can be obtained.

Using this new framework, Drischler *et al.* (75, 64) studied the EFT convergence of the first order-by-order calculations with NN and 3N interactions up to N³LO in PNM and SNM, conducted in Refs. (27, 77) using a novel Monte Carlo integration framework for MBPT. The associated N³LO 4N Hartree-Fock energies have been found negligible compared to the overall uncertainties (see also Ref. (78)). To construct a set of order-by-order NN and 3N interactions up to N³LO, Ref. (27) adjusted the two 3N LECs to the triton and (n_0, E_0) for two cutoffs. Several potentials with reasonable saturation properties were obtained, although generally underbound at N³LO. This holds also at the 2σ credibility level with EFT truncation errors quantified (64), as depicted by the ellipses “GP–B Λ [MeV]” in Fig. 2 (right). Hoppe *et al.* (79) found that, in agreement with the expectations from SNM, predicted values for the corresponding binding energies of medium-mass nuclei are too small compared with experiment and, in contrast to the SNM expectations, predicted values for the corresponding charge radii are too large. Since both observables were also much more sensitive to the 3N LEC c_D , SNM and medium-mass nuclei seem more intricately connected than one might naively expect (79).

Figure 3 shows the order-by-order predictions for the energy per particle, pressure, and speed of sound squared in PNM at the 1σ confidence level based on “GP–B 500” (75).

⁷For instance, $y_{\text{ref}} \simeq y_0$ and $Q \sim p/\Lambda_b$ with the typical momentum $p \propto k_F(n)$ and some estimate of the EFT breakdown scale Λ_b have been used to estimate uncertainties in the nuclear EOS.

⁸The framework is publicly available at <https://buqeeye.github.io/software/>.

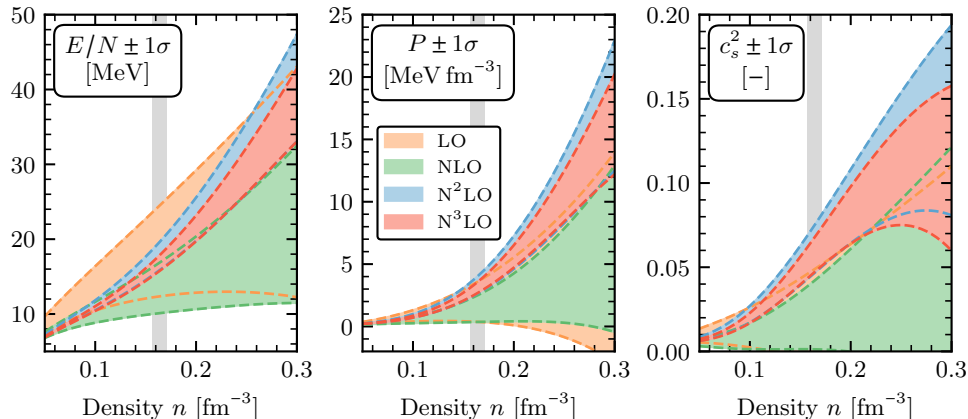


Figure 3: Order-by-order predictions for the energy per particle E/N (left panel), pressure $P = n^2 d(E/N)/dn$ (middle panel), and speed of sound squared $c_s^2 = \partial P/\partial \varepsilon$ (right panel) in PNM as a function of the density (75) based on the MBPT calculations up to N³LO in Ref. (27). The energy density $\varepsilon = n(E/N + m_n)$ includes the neutron rest mass energy m_n . Correlated uncertainty bands are given at the 1σ confidence level. The data were taken from Ref. (75).

The observables show an order-by-order convergence pattern at $n \lesssim 0.1 \text{ fm}^{-3}$, whereas N²LO and N³LO have a markedly different density dependence at $n \gtrsim n_0$ due to repulsive 3N contributions. This is also manifested in the Bayesian diagnostics (73). Assuming $Q = k_F/\Lambda_b$, the inferred breakdown scale $\Lambda_b \approx 600 \text{ MeV}$ is consistent with free-space NN scattering and could be associated with $n > 2n_0$. The EFT truncation errors are strongly correlated in density and to those in SNM. A correlated approach is therefore necessary to propagate uncertainties reliably to derived quantities, although the standard EFT uncertainty for the energy per particle is broadly similar to the 1σ confidence level (75).

3.2. Nuclear symmetry energy and the isospin-asymmetry expansion

The nuclear symmetry energy is a key quantity to understand the structure of neutron-rich nuclei and neutron stars. Although masses of heavy nuclei constrain the value of the symmetry energy well at nuclear densities, its density dependence is much less known (94). Studying the density-dependent symmetry energy from theory, experiment, and observation is therefore an important task in the era of multimessenger astronomy.

Figure 4 (left) summarizes theoretical constraints for $E_{\text{sym}}(n \leq 2n_0)$ from a wide range of chiral NN and 3N forces as well as different many-body methods. Specifically, we show the results for $E_{\text{sym}}(n) = E(n, \delta = 1)/A - E(n, 0)/A$ as obtained in the calculations by Lim & Holt (83) and Drischler *et al.* (64, 27) [“GP-B 500”] in MBPT, Carbone *et al.* (44) in the SCGF method, and Lonardonì *et al.* (49) using QMC methods. The latter were conducted with two different parameterizations of the N²LO 3N contact interaction (*i.e.*, distinct bands for E_1 and E_τ) to demonstrate the significant regulator artifacts present in local chiral 3N potentials. Different uncertainty estimates were used in these calculations. The uncertainty bands by Carbone *et al.* probe parameter variations in the nuclear interactions, while those by Lonardonì *et al.* and Drischler *et al.* quantify truncation errors using the standard

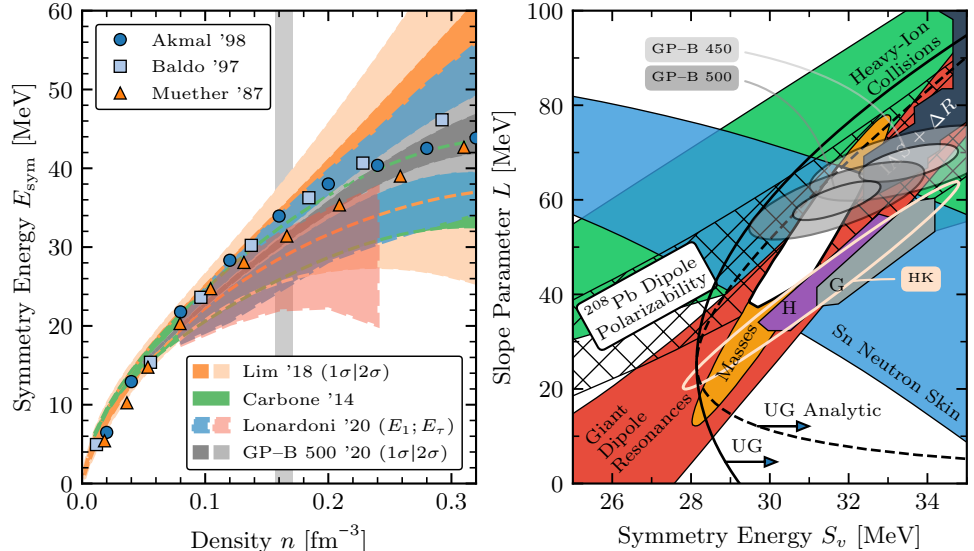


Figure 4: (left) Constraints on $E_{\text{sym}}(n)$ based on chiral interactions (bands) and phenomenological potentials (symbols). The vertical band depicts the empirical saturation density. Dashed lines are used to enhance readability. Data were taken from Akmal *et al.* (80), Baldo *et al.* (81), Muether *et al.* (82), Lim & Holt (83), Carbone *et al.* (44), Lonardoni *et al.* (49), and Drischler *et al.* (64, 27) [“GP-B 500”]. (right) Theoretical and experimental constraints for (S_v, L) as well as the conjectured UG bounds (84) in comparison (see annotations in the panel). The experimental constraints are derived from heavy-ion collisions (HIC) (85), neutron-skin thicknesses of Sn isotopes (86), giant dipole resonances (GDR) (87), the dipole polarizability of ^{208}Pb (88, 89), nuclear masses (90), and isobaric analog states and isovector skins (IAS + ΔR) (91). In addition, theoretical constraints derived from microscopic neutron-matter calculations by Hebeler *et al.* (H) (92), Holt & Kaiser (HK) (39), and Gandolfi *et al.* (G) (93). Gray ellipses (64) show the allowed regions from PNM and SNM calculations at N³LO with truncation errors quantified (light: 1 σ , dark: 2 σ). The white area in the center shows the joint experimental constraint; the constraints extracted from measurements of IAS + ΔR are not included in this area because they barely overlap.

EFT uncertainty (up to N²LO) and BUQEYE’s new Bayesian framework (up to N³LO), respectively. Also many-body (or statistical Monte Carlo) uncertainties are included in the bands. Lim & Holt performed a statistical analysis of MBPT calculations based on a range of chiral potentials at different orders and two single-particle spectra to probe the chiral and many-body convergence. Only the results by Lim & Holt and Drischler *et al.* (both MBPT) have a clear statistical interpretation, each at the 1 σ and 2 σ confidence level (different shadings). Overall, the constraints from ChEFT are consistent with each other, even at the highest densities shown, but the uncertainties in $E_{\text{sym}}(n)$ are generally sizable, *e.g.*, 20.7 ± 1.1 , 31.5 ± 3.0 , and 49.0 ± 12.0 MeV at $n_0/2$, n_0 , and $2n_0$, respectively, for Lim & Holt at the 1 σ confidence level. Drawing general conclusions from comparing the sizes of these bands can be misleading since the underlying methods for estimating uncertainties

are quite different. Order-by-order comparisons for a wider range of chiral NN and 3N interactions with EFT truncation errors quantified are called for to provide more insights in and stringent constraints on $E_{\text{sym}}(n)$. The Bayesian statistical tools introduced by the BUQEYE Collaboration allow for such systematic studies.

Despite the large uncertainties in the SNM EOS (see Sec. 3.1), predictions for $E_{\text{sym}}(n)$ [as an energy difference] can be made with significantly smaller uncertainties than those in $E(n, 1)/A$ and $E(n, 0)/A$ individually, if correlations are properly considered. The BUQEYE Collaboration (64) found that the EFT truncation errors associated with the PNM and SNM calculations in Ref. (27) are *highly correlated*, meaning that the uncertainty in $E_{\text{sym}}(n)$ is less than the usual in-quadrature sum of errors. Combined with order-by-order calculations up to N³LO this led to the narrow constraints [see gray bands in Fig. 4 (left)] based on the interactions used with $\Lambda = 500$ MeV (*e.g.*, $E_{\text{sym}}(2n_0) = 45.0 \pm 2.8$ MeV). Another set with $\Lambda = 450$ MeV is compatible at the 2σ confidence level. The bands agree with the constraints by Lim & Holt at the 1σ level (or even better) as well as the calculations by Akmal *et al.* (80), Baldo *et al.* (81), and Muether *et al.* (82) with phenomenological nuclear potentials. The latter, however, do not provide uncertainties that could be used to judge the level of agreement. These correlations need to be investigated further using different many-body frameworks and interactions.

Figure 4 (right) compares various theoretical and experimental constraints in the S_v - L plane (see annotations). The regions obtained by Hebeler *et al.* (92, “H”), Gandolfi *et al.* (93, “G”), and Holt & Kaiser (39, “HK”), which were derived from microscopic PNM calculations and the empirical saturation point, agree well with each other and are consistent with the range in S_v of the joint experimental constraint (white area), although L is predicted with somewhat lower values. The 1σ and 2σ ellipses of “GP-B 500” (as in Fig. 4 (left)) are in excellent agreement with the joint experimental constraint [“GP-B 450” is slightly shifted to higher (S_v, L)], indicating a stiffer neutron-rich matter EOS at n_0 compared to the other theoretical constraints. This is, however, consistent with joint theory-agnostic posteriors from pulsar, gravitational-wave, and NICER observations (*e.g.*, compare with Figure 1 in Ref. (95)). An important feature of the correlated GP approach is that the theoretical uncertainties in n_0 (including truncation errors) are accounted for through marginalization over the Gaussian posterior for the saturation density predicted from the SNM calculations, $\text{pr}(n_0) \approx 0.17 \pm 0.01 \text{ fm}^{-3}$. Apart from the calculations by Holt & Kaiser (“HK”) allowing slightly lower (S_v, L) , all shown theory calculations satisfy the constraint (solid black line) derived from the conjecture (84) that the unitary gas (UG) sets a lower bound for the PNM EOS. [Note that Ref. (84) also made additional assumptions to derive an analytic bound (dashed black line).] Overall, Fig. 4 (right) shows that current constraints from nuclear theory and experiment predict the symmetry energy parameters in the range $S_v \approx 28 - 35$ MeV and $L \approx 20 - 72$ MeV.

UG: unitary gas

While the standard quadratic approximation [$E(n, \delta)/A = E(n, 0)/A + E_{\text{sym}}(n) \delta^2$] is in general sufficient to characterize the isospin-asymmetry dependence of the nuclear EOS, certain neutron-star properties, such as the crust-core transition (96) and the threshold for the direct URCA cooling process (97), are sensitive to nonquadratic contributions. Neglecting charge-symmetry breaking effects, the energy per particle may be assumed to have an expansion in the asymmetry δ of the form $E(n, \delta)/A \approx E(n, 0)/A + \sum_{l=1}^L S_{2l}(n) \delta^{2l}$, where the standard quadratic approximation corresponds to $S_{2l>2}(n) = 0$. Note, however, that already the FFG contributes to the nonquadratic terms, *e.g.*, $S_4^{\text{FFG}}(n) \simeq 0.45 \text{ MeV} \times (n/n_0)^{2/3}$. Parametric fits to microscopic ANM calculations have been used to investi-

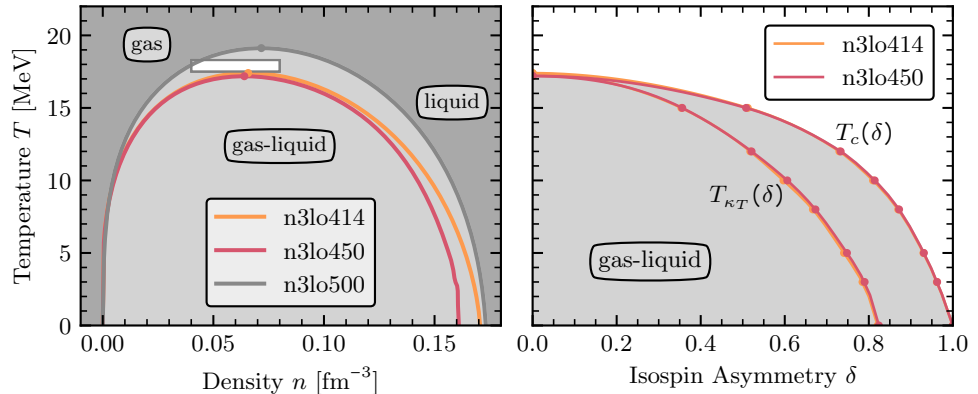


Figure 5: (left) Liquid-gas coexistence boundary (binodal) of SNM from second-order MBPT calculations based on three sets of $N^3\text{LO}$ NN potentials and $N^2\text{LO}$ 3N interactions with $\Lambda = 414, 450,$ and 500 MeV (38, 55). The zero-temperature limit of the coexistence boundary corresponds to the nuclear saturation point. The white box shows the empirical range for the critical point from Ref. (101). (right) Asymmetry dependence of the critical temperature $T_c(\delta)$ and the temperature $T_{\kappa_T}(\delta)$ where the region with negative κ_T^{-1} vanishes.

gate the nonquadratic contributions and found them to be relatively small (56, 68, 98, 69). Recently, however, Kaiser (99) has shown that MBPT at second order gives rise to additional logarithmic contributions $\sim \delta^{2l} \ln |\delta|$ with $l \geq 2$. Furthermore, Wellenhofer *et al.* (69) found that the analogous expansion of the free energy exhibits convergent behavior for $\delta \leq 1$ only at high temperature. That is, the expansion's radius of convergence decreases to zero in the limit $T \rightarrow 0$ (with diverging $S_{2l>2}$), as implied by the logarithmic terms at $T = 0$. Nevertheless, Wen & Holt (100) demonstrated that the coefficients of the normal and logarithmic terms at $T = 0$ can be extracted up to $\mathcal{O}(\delta^6)$ from high-precision MBPT calculations with chiral interactions. Such calculations allow for the improvement of existing parametrizations in δ at $T = 0$ and help motivate the investigation of alternative schemes, such as an expansion in terms of the proton fraction $x = n_p/n = (1 - \delta)/2$ for neutron-rich matter.

3.3. Nuclear thermodynamics

While thermal effects are negligible in isolated neutron stars, they become important in neutron star mergers and core-collapse supernovae, where $T \lesssim 100$ MeV can be reached. Dense matter at such high temperatures not only consists of nucleons and leptons but also of additional particles such as pions and hyperons. The consistent inclusion of these particles in medium is work in progress (102, 103). In the nascent field of multimessenger astronomy, one of the immediate theoretical needs is consistent modeling of (i) cold neutron stars, (ii) hot hypermassive neutron stars formed in the aftermath of compact object mergers, and (iii) core-collapse supernovae so that observations and simulations in any one of these astrophysical regimes can be propagated to constrain the others. Finite-temperature MBPT with ChEFT interactions is a suitable framework for this purpose, and here we describe some of the results on nuclear thermodynamics in recent years (for reviews, see Refs. (104, 105)).

The salient thermodynamic feature of homogeneous nuclear matter at sub-saturation densities is the presence of a liquid-gas type instability toward the formation of clustered structures. In neutron stars, this instability corresponds to the crust-core transition, involving such intricate features as a variety of “pasta” shapes (106). The nuclear liquid-gas instability is also connected to the observed multifragmentation events in intermediate-energy heavy-ion collisions. In the idealized case of (infinite) nuclear matter, there is a liquid-gas phase transition of van-der-Waals type. Nuclear matter calculations at finite temperature with chiral interactions have provided predictions for the properties of this phase transition, in particular the location of the critical point. Figure 5 (left) shows the second-order MBPT results for the boundary of the liquid-gas coexistence region (so-called binodal) of SNM obtained in Ref. (38). [The results for the binodal of SNM recently obtained with the SCGF method (45) and lattice EFT (41) are similar to those in Fig. 5.] The predicted critical point, especially the associated temperature $T_c \approx 17 - 19$ MeV, is consistent with estimates (*e.g.*, $T_c \approx 15 - 20$ MeV (107)) extracted from multifragmentation, nuclear fission, and compound nuclear decay experiments (107, 101).

In the interior of the binodal a region where the homogeneous system is unstable with respect to infinitesimal density fluctuations can be found. The boundary of this region is called spinodal. Between the binodal and spinodal the uniform system is metastable. [The two boundaries coincide at the critical point.] For SNM, the unstable region is identified by a negative inverse isothermal compressibility, $\kappa_T^{-1} = n(\partial P/\partial n) < 0$. An equivalent stability criterion is $\partial\mu/\partial n > 0$, corresponding to a strictly convex free energy density $\mathcal{F}(T, n)$ as a function of n . If charge-symmetry breaking effects are neglected, SNM can be treated as a pure substance with one particle species (nucleons), whereas ANM is a binary mixture with two thermodynamically distinct particles (neutrons and protons). This implies that the stability criteria are different in the two cases, and for ANM the region with $\kappa_T^{-1} < 0$ is a subregion of the spinodal region. There are various equivalent stability criteria for binary mixtures (108). A useful criterion is that outside the spinodal the free energy $\mathcal{F}(T, n_n, n_p)$ is a strictly convex function of n_n and n_p (see Ref. (55) for details). The MBPT results for the asymmetry dependence of the critical temperature $T_c(\delta)$ from Ref. (55) are shown in Fig. 5 (right). For comparison, we also show the trajectory of the temperature $T_{\kappa_T}(\delta)$ where the subregion with negative κ_T^{-1} vanishes. The trajectory of $T_c(\delta)$ reaches its $T = 0$ endpoint at a small proton fraction x ; *i.e.*, while PNM is stable at all densities, already small x lead to a region where the system undergoes a phase separation (55, 109).

A useful characteristic for the temperature dependence of the nuclear EOS is the thermal index $\Gamma_{\text{th}}(T, n, \delta) = 1 + P_{\text{th}}(T, n, \delta)/\mathcal{E}_{\text{th}}(T, n, \delta)$, where P_{th} is the thermal part of the pressure, and \mathcal{E}_{th} is the thermal energy density. For a free gas of nucleons with effective masses $m_{n,p}^*(n, \delta)$ one obtains for Γ_{th} the following temperature-independent expression⁹

$$\Gamma_{\text{th}}^*(n, \delta) = \frac{5}{3} - \sum_{t=n,p} \frac{n_t(n, \delta)}{m_t^*(n, \delta)} \frac{\partial m_t^*(n, \delta)}{\partial n}. \quad (8)$$

[To be precise, for $\delta \notin \{0, 1\}$ the above expression is valid only in the classical limit, but it provides a good approximation to $\Gamma_{\text{th}}^*(n, x)$ for intermediate values of δ as Ref. (67) showed.] Recently, Refs. (25, 110) showed that $\Gamma_{\text{th}}^*(n, \delta)$ reproduces the exact Γ_{th} with high accuracy. This implies that the temperature-dependence of the EOS can be characterized in terms of

⁹The thermal index of a free Fermi gas is $\Gamma_{\text{th,free}} = 5/3$.

a temperature-independent effective mass (see Ref. (67) for a recent implementation), which is in particular useful for monitoring thermal effects in astrophysical applications (111, 112).

4. Applications to neutron star physics

In this Section our goal is to emphasize the prominent role of nuclear theory in modeling neutron stars, core-collapse supernovae, and neutron star mergers. We begin by placing high-energy nuclear astrophysics in the more general context of the QCD phase diagram and discuss under what ambient conditions ChEFT can serve as a tool to constrain the properties of hot and dense matter. Specific applications include the neutron-star mass-radius relation, moment of inertia, and tidal deformability, as well as the nuclear EOS and neutrino opacity for astrophysical simulations.

4.1. Scales in hot and dense stellar matter

The extreme astrophysical environments found in core-collapse supernovae, neutron star interiors, and neutron-star mergers span baryon number densities $n_B \sim 10^{-7} - 10^1 n_0$, temperatures $T \sim 0 - 100$ MeV, and isospin asymmetries $\delta \sim 0 - 1$ (corresponding to electron fractions $Y_e \sim 0 - 0.5$) (113). In Sections 2 and 3 we have shown that ChEFT provides a suitable framework to constrain the EOS, transport, and response properties of hadronic matter when the physical energy scale is well below the chiral symmetry breaking scale of $\Lambda_\chi \sim 1$ GeV. In practice, ChEFT descriptions of nuclear matter based on high-precision NN and 3N forces begin to break down at densities $n \approx 2 - 3 n_0$ and temperatures $T \lesssim 30$ MeV. Therefore, additional modeling is needed at high densities and temperatures to cover all regions of astrophysical interest. For this purpose, high-energy heavy-ion collisions at RHIC, LHC, and especially FAIR aim to probe states of matter similar to those that exist naturally in neutron stars, but reaching sufficiently large proton-neutron asymmetries remains a significant challenge that may be addressed with next-generation radioactive ion beam facilities, such as FRIB. The interplay of microscopic ChEFT, whose convergence pattern is not especially sensitive to the isospin asymmetry, together with upcoming nuclear experiments that create and study hot, dense, and neutron-rich matter, will provide a direct line of inquiry probing neutron-star physics from low to high densities.

From the observational side, measurements of neutron star masses, radii, tidal deformabilities, and moments of inertia are expected to place constraints on the pressure of beta-equilibrium matter at $n \gtrsim 2n_0$ (114, 83, 115). In Fig. 6, we present a qualitative overview of the QCD phase diagram and highlight regions probed by nuclear experiments (RHIC, LHC, FAIR, and FRIB), theory (lattice QCD and ChEFT), and astrophysical simulations of neutron stars, supernovae, and neutron star mergers. We see that ChEFT intersects strongly with the region of FRIB experiments and nuclear astrophysics, providing a bridge between new discoveries in the laboratory and their implications for neutron stars. The next decade is expected to witness a strong interplay among all of these different fields, with nuclear theory predictions getting confronted with stringent empirical tests.

4.2. Neutron star structure

The mass-radius relation of non-rotating neutron stars is determined from the EOS by the general relativistic equations for hydrostatic equilibrium, the Tolmann-Oppenheimer-

RHIC: Relativistic Heavy Ion Collider

LHC: Large Hadron Collider

FAIR: Facility for Antiproton and Ion Research

FRIB: Facility for Rare Isotope Beams

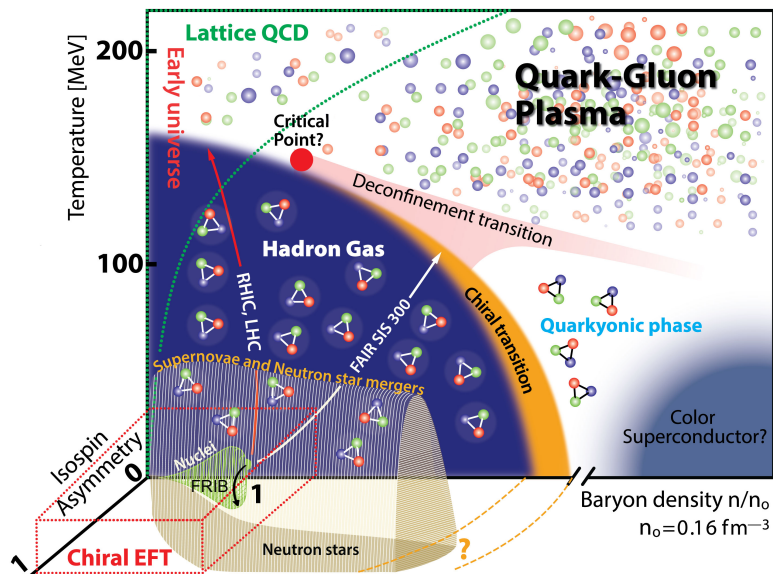


Figure 6: Schematic view of the QCD phase diagram. We highlight regions probed by experiments (RHIC, LHC, FAIR, and FRIB), regions of validity for lattice QCD and ChEFT, and environments reached in neutron stars, supernovae, and neutron star mergers.

Volkoff (TOV) equations:

$$\frac{dp}{dr} = -\frac{G(M(r) + 4\pi r^3 p)(\varepsilon + p)}{r(r - 2GM(r))}, \quad \frac{dM}{dr} = 4\pi r^2 \varepsilon, \quad (9)$$

where r is the radial distance from the center of the star, $M(r)$ is the mass enclosed within r , ε is the energy density, and p is the pressure. Analysis of spectral data from neutron stars in quiescent low-mass x-ray binaries and x-ray bursters (116, 117) have resulted in radius measurements $R_{1.5} = 10\text{--}13$ km for typical $1.5 M_{\odot}$ neutron stars. More recently, the NICER x-ray telescope has observed hot spot emissions from the accretion-powered x-ray pulsar PSR J0030+045. Pulse profile modeling of the x-ray spectrum from two independent groups have yielded consistent results for the neutron star's mass $M = 1.44^{+0.15}_{-0.14} M_{\odot}$ (118) and $M = 1.34^{+0.15}_{-0.16} M_{\odot}$ (119) and radius $R = 13.02^{+1.24}_{-1.06}$ km (118) and $R = 12.71^{+1.14}_{-1.19}$ km (119) at the 68% credibility level. Future large area x-ray timing instruments, such as STROBE-X and eXTP, have the potential to reduce uncertainties in the neutron-star mass-radius relation to $\sim 2\%$ at a given value of the mass. This would significantly constrain the neutron-rich matter EOS at $n \approx 2n_0$ and when combined with mass and radius measurements of the heaviest neutron stars could give hints about the composition of the inner core (120).

In recent years numerous works have studied constraints on the neutron star EOS from ChEFT.¹⁰ In Ref. (92) the EOS of neutron-rich matter was calculated up to saturation

¹⁰In addition to a high-density extrapolation, a uniform-matter EOS from ChEFT needs to be supplemented with a neutron-star crust model, *e.g.*, the BPS crust model (121).

TOV: Tolmann-Oppenheimer-Volkoff

NICER: Neutron star Interior Composition Explorer

STROBE-X: Spectroscopic Time-Resolving Observatory for Broadband Energy X-rays

eXTP: enhanced X-ray Timing and Polarimetry

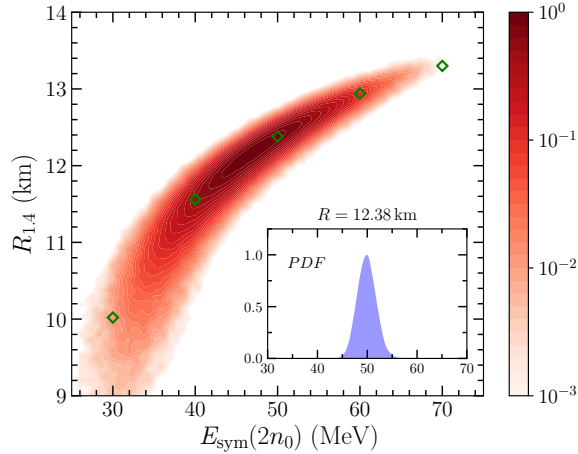


Figure 7: Correlations between the radius of a $1.4 M_{\odot}$ neutron star and the isospin asymmetry energy E_{sym} at twice saturation density $n = 2n_0$. The inset shows the probability distribution function (PDF) of $E_{\text{sym}}(2n_0)$ for the specific value $R_{1.4} = 12.38$ km. Results obtained from the Bayesian modeling of the nuclear EOS in Ref. (83).

density with MBPT using chiral NN and 3N interactions. To extrapolate to higher densities, a series of piecewise polytropes was used to parameterize the EOS. It was found that ChEFT generically gives rise to soft EOSs that lead to $1.4 M_{\odot}$ neutron stars with radii in the range $R_{1.4} = 10 - 14$ km. Subsequent studies (*e.g.*, Refs. (122, 123, 124, 67)) have employed a wider range of chiral forces, increased the assumed range of validity for ChEFT calculations to $2n_0$, and explored other high-density EOSs, including smooth extrapolations and speed of sound parameterizations. The choice of transition density at which ChEFT predictions are replaced by model-dependent high-density parameterizations has a particularly large influence on neutron-star radius constraints. For instance, when the transition density was raised to $n_t = 2n_0$, Ref. (125) obtained $R_{1.4} = 9.4 - 12.3$ km while Ref. (124) found $R_{1.4} = 10.3 - 12.9$ km, both calculations eliminating the stiffest EOSs that would give rise to $R_{1.4} > 13$ km. To demonstrate how a precise neutron-star mass and radius measurement can constrain the EOS of beta-equilibrium matter at $n = 2n_0$, in Fig. 7 we show the correlated probability distribution (83) for the radius of a $1.4 M_{\odot}$ neutron star and the nuclear symmetry energy at twice saturation density $E_{\text{sym}}(2n_0)$. In the inset we show the conditional probability distribution for $E_{\text{sym}}(2n_0)$ assuming a precise measurement of $R_{1.4} = 12.38$ km. For the specific EOS modeling used in Ref. (83), such a precise radius constraint determines $E_{\text{sym}}(2n_0)$ with an uncertainty of approximately 10%.

In addition to radius measurements, there has long been the possibility (126, 127) of obtaining a neutron-star moment of inertia measurement based on long-term radio timing of PSR J0737-3039, a binary pulsar system in which the periastron advance receives a small correction from relativistic spin-orbit coupling. A recent analysis (128) has shown that by 2030 a moment of inertia measurement of PSR J0737-3039A to 11% precision at the 68% confidence level will be achievable. The moment of inertia for a uniformly rotating neutron star of radius R and angular velocity Ω can be calculated in the slow-rotation approximation, valid for most millisecond pulsars, by solving the TOV equations together

with

$$I = \frac{8\pi}{3} \int_0^R r^4 (\varepsilon + p) e^{(\lambda-\nu)/2} \frac{\bar{\omega}}{\Omega} dr, \quad e^{-\lambda} = \left(1 - \frac{2m}{r}\right)^{-1}, \quad \frac{d\nu}{dr} = -\frac{2}{\varepsilon + p} \frac{dp}{dr}, \quad (10)$$

where λ and ν are metric functions and $\bar{\omega}$ is the rotational drag. In Refs. (129, 130) the moment of inertia of PSR J0737-3039A, which has a very well measured mass of $M = 1.338 M_\odot$, was calculated from EOSs based on ChEFT. In Ref. (129) it was found that at the 95% credibility level, the moment of inertia of J0737-3039A lies in the range $0.98 \times 10^{45} \text{ g cm}^2 < I < 1.48 \times 10^{45} \text{ g cm}^2$, while Ref. (130) found a consistent but somewhat larger range of $1.06 \times 10^{45} \text{ g cm}^2 < I < 1.70 \times 10^{45} \text{ g cm}^2$. The moment of inertia is strongly correlated with the neutron star radius, and it has been shown (131) that measurements of the PSR J0737-3039A moment of inertia can constrain its radius to within $\pm 1 \text{ km}$.

In the past ten years, several neutron stars (132, 133, 134) with well measured masses of $M \gtrsim 2 M_\odot$ have been observed. The maximum mass ($M_{\text{max}}^{\text{TOV}}$) of a non-rotating neutron star is a key quantity to probe the composition of the inner core, which must have a sufficiently stiff EOS to support the enormous pressure due to the outer layers.¹¹ To date the strongest candidate for the heaviest measured neutron star is PSR J0740+6620, with a mass of $M = 2.14_{-0.18}^{+0.20} M_\odot$ at the 95% credibility level (134). As mentioned previously, ChEFT generically gives rise to relatively soft EOSs just above nuclear saturation density. The existence of a very massive neutron star with $M = 2.14 M_\odot$ would require a stiff EOS at high densities, revealing a slight tension with ChEFT (136). However, even smooth extrapolations (83, 67) of EOSs from ChEFT can produce maximum neutron star masses in the range $2.0 M_\odot \lesssim M_{\text{max}}^{\text{TOV}} \lesssim 2.4 M_\odot$, and therefore more precise radius measurements (or the observation of heavier neutron stars) are needed to make strong inferences about the EOS in the ChEFT validity region $n \lesssim 2n_0$.

4.3. Neutron star mergers

The advent of gravitational wave astronomy has opened a new window into the visible Universe. Current gravitational wave detectors (LIGO and Virgo) are sensitive to frequencies $10 \text{ Hz} < f < 10 \text{ kHz}$, which is the prime range for compact object mergers and supernovae. Gravitational wave astronomy therefore has major implications for the field of nuclear astrophysics (3). In particular, during the late-inspiral phase of binary neutron star coalescence, a pre-merger neutron star will deform with induced quadrupole moment Q under the large tidal gravitational field \mathcal{E} : $Q_{ij} = -\lambda \mathcal{E}_{ij}$, where λ is the dimensionful tidal deformability parameter. Tidal deformations enhance gravitational radiation and increase the rate of inspiral. Gravitational wave detectors are sensitive to such phase differences and hence the dense matter EOS, but such corrections enter formally at fifth order (137) in a post-Newtonian expansion of the waveform phase and are therefore difficult to extract. The tidal deformability is an important observable in its own right, but this quantity is also strongly correlated with both the neutron star radius (138), since more compact stars experience a smaller deformation under a given tidal field, and especially the moment of inertia through the celebrated I-Love-Q relations (139). The post-merger gravitational wave signal from binary neutron star coalescence can also carry important information on the nuclear

¹¹Beyond $M_{\text{max}}^{\text{TOV}}$, additional stable branches (135), such as hybrid quark-hadron stars or pure quark stars, may appear before the ultimate collapse to a black hole.

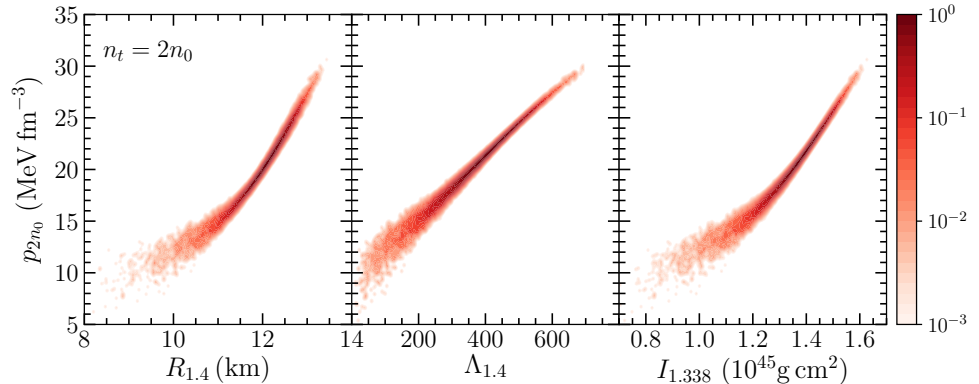


Figure 8: Joint probability distribution for the pressure of beta-equilibrium matter $p(2n_0)$ with the radius of a $1.4 M_\odot$ neutron star (left), the tidal deformability of a $1.4 M_\odot$ neutron star (middle), and the moment of inertia of PSR J0737-3039A with a mass of $1.338 M_\odot$ (right). Results obtained from the Bayesian modeling of the nuclear EOS in Ref. (83).

LIGO: Laser Interferometer Gravitational-Wave Observatory

EOS. It has been shown (140) that the peak oscillation frequency f_{peak} of a neutron-star merger remnant is strongly correlated with neutron star radii. Moreover, a strong first-order phase transition can show up as a deviation in the empirical correlation band between f_{peak} and Λ (141).

The first observation (142), GW170817, of a neutron star merger through its gravitational wave emissions was accompanied by a short gamma-ray burst and optical counterpart (143). The combined multi-messenger observations of this single event have resulted in a wealth of new insights about the origin of the elements and the properties of neutron stars. Analysis of the gravitational waveform resulted in a prediction (144) $\Lambda_{1.4} = 190_{-120}^{+390}$ for the dimensionless tidal deformability $\Lambda = \lambda/M^5$ of a $1.4 M_\odot$ neutron star. Theoretical predictions from ChEFT (83, 145) predating the analysis in Ref. (144) yielded similarly small tidal deformabilities $140 < \Lambda < 520$ (83). Analogous constraints on the binary tidal deformability parameter

$$\tilde{\Lambda} = \frac{16}{13} \frac{(m_1 + 12m_2)m_1^4\Lambda_1 + (m_2 + 12m_1)m_2^4\Lambda_2}{(m_1 + m_2)^5} \quad (11)$$

from gravitational-wave data [$\tilde{\Lambda} = 300_{-230}^{+420}$ (146)] and ChEFT [$80 < \tilde{\Lambda} < 580$ (145)] were similarly consistent. From the strong correlation between neutron star radii and tidal deformabilities, the LIGO/Virgo Scientific Collaboration reported (144) an inferred constraint of $R = 11.9_{-1.4}^{+1.4}$ km for both of the neutron stars involved in the merger under the assumption that the shared EOS could support $2 M_\odot$ neutron stars. Only the combined mass $M_{\text{tot}} = 2.74_{-0.01}^{+0.04} M_\odot$ of the binary was very well measured from the gravitational waveform, but neither of the individual component masses $1.17 M_\odot < M_{1,2} < 1.60 M_\odot$ were expected (142) to deviate more than 20% from the canonical value of $M \simeq 1.4 M_\odot$, assuming low neutron star spins. In summary, GW170817 data were found to strongly favor the soft EOSs predicted from ChEFT, though many other models (147) with generically stiffer EOSs were consistent with the upper bounds on Λ and $R_{1.4}$ from GW170817.

Current gravitational wave interferometers do not have large signal-to-noise ratios at the high frequencies expected during the post-merger ringdown phase and therefore GW170817

provided no clues about the fate of the merger remnant. Nevertheless, an analysis of the spectral and temporal properties of the kilonova (148) optical counterpart to GW170817 have been used (149, 150, 151, 152, 153) to infer the lifetime of the merger remnant. Depending on the component neutron star masses prior to merger (primarily the total mass M_{tot}) as well as the maximum mass for a nonrotating neutron star $M_{\text{max}}^{\text{TOV}}$, the merger remnant can (i) undergo immediate collapse to a black hole, (ii) exist as a short-lived hypermassive neutron star supported against collapse by differential rotation, (iii) persist as a longer-lived supramassive neutron star supported against collapse by rigid-body rotation, or (iv) form a stable massive neutron star. While there is still some uncertainty about what ranges of M_{tot} will lead to each of the above four scenarios, it has been suggested (150) that prompt collapse will occur when $M_{\text{tot}} \gtrsim 1.3 - 1.6 M_{\text{max}}^{\text{TOV}}$, hypermassive neutron stars will be created when $1.2 M_{\text{max}}^{\text{TOV}} \lesssim M_{\text{tot}} \lesssim 1.3 - 1.6 M_{\text{max}}^{\text{TOV}}$, and supramassive neutron stars will result when $M_{\text{tot}} \lesssim 1.2 M_{\text{max}}^{\text{TOV}}$. Each merger outcome is expected to have a qualitatively different optical counterpart and total mass ejection, since longer remnant lifetimes generically give rise to more and faster moving disk wind ejecta.

Observations of the GW170817 kilonova suggest that the most likely outcome of the neutron star merger was the formation of a hypermassive neutron star, which would imply a value of $M_{\text{max}}^{\text{TOV}} = 2.15 - 2.35 M_{\odot}$ (151, 150, 153). Eliminating the possibility of prompt black hole formation in GW170817 also rules out compact neutron stars with small radii and tidal deformabilities. In Ref. (149) such arguments were used to infer that the radius of a $1.6 M_{\odot}$ neutron star must be larger than $R_{1.6} \gtrsim 10.7 \text{ km}$, while in Ref. (152) it was found that the binary tidal deformability parameter for the GW170817 event must satisfy $\tilde{\Lambda} \gtrsim 400$. Both of these inferred constraints are compatible with predictions (83, 145, 124, 123) from ChEFT. However, the constraint on the binary tidal deformability $\tilde{\Lambda} > 400$ can rule out a significant set of soft EOSs (154), roughly half of those allowed in the analysis of Ref. (83). Combined gravitational wave and electromagnetic observations of binary neutron star mergers together with more precise radius measurements therefore have the possibility to strongly constrain the dense matter EOS and related neutron star properties in the regime of validity of ChEFT (154, 155, 156). As a demonstration, in Fig. 8 we show the joint probability distributions (83) for the pressure of nuclear matter at $n = 2n_0$ with (i) the radius of a $1.4 M_{\odot}$ neutron star, (ii) the tidal deformability of a $1.4 M_{\odot}$ neutron star, and (iii) the moment of inertia of PSR J0737-3039A with a mass of $1.338 M_{\odot}$.

4.4. Core-collapse supernovae

Neutron stars are born following the gravitational collapse and ensuing supernova explosion of massive stars ($M \gtrsim 8 M_{\odot}$). The core bounce probes densities only slightly above normal nuclear saturation density (113) and leaves behind a hot ($T \sim 20 - 50 \text{ MeV}$) nascent proto-neutron star. During the subsequent Kelvin-Helmholtz phase that lasts tens of seconds, the proto-neutron star emits neutrinos, cools to temperatures $T < 5 \text{ MeV}$, de-leptonizes, and contracts to reach supra-saturation densities in the innermost core. The success or failure of the supernova itself (157), the thermal and chemical evolution during the Kelvin-Helmholtz phase (158), and the possibility of novel nucleosynthesis in the neutrino-driven wind (159) depend on details of the nuclear EOS and weak reaction rates.

Investigating the qualitative impact of specific EOS properties, such as the incompressibility or the symmetry energy, on the fate of supernova explosions is often challenging due to “Mazurek’s Law”, a colloquial observation that feedback effects tend to wash out any

fine tuning of parameters in core-collapse supernovae (160). Nevertheless, several recent systematic investigations (161, 111) of EOS parameters have supported the idea that a high density of states, linked to a large value of the in-medium nucleon effective mass M^* , reduces thermal pressure and leads to enhanced contraction of the initial proto-neutron star. This results in the emission of higher-energy neutrinos that support the explosion through the neutrino reheating mechanism (157). Since microscopic calculations based on ChEFT tend to predict larger values of the effective mass than many mean-field models (162, 110), these observations help motivate recent efforts (163, 67) to include thermal constraints from ChEFT directly into supernova EOS tables.

Neutrino reactions also affect the nucleosynthesis outcome in neutrino-driven wind outflows and the late-time neutrino signal that will be measured with unprecedented detail during the next galactic supernova. Charged-current neutrino-absorption reactions $\nu_e + n \rightarrow p + e^-$ and $\bar{\nu}_e + p \rightarrow n + e^+$, which can be calculated from the imaginary part of vector and axial vector response functions, are especially sensitive (164, 165) to nuclear interactions and in particular the difference $\Delta U = U_n - U_p$ between proton and neutron mean fields. The isovector mean field is especially important in the neutrinosphere, the region of warm and dense matter where neutrinos decouple from the exploding star. Recently, the calculation (166, 162) of nuclear response functions that include mean-field effects from ChEFT interactions have shown that terms beyond the Hartree-Fock approximation are needed for accurate modeling. In particular, resummed particle-particle ladder diagrams were shown (166) to produce larger isovector mean fields due to resonant, non-perturbative effects in the NN interaction. Moreover, for neutral-current neutrino reactions, such as neutrino pair bremsstrahlung and absorption, resonant NN interactions were shown to significantly enhance reaction rates at low densities compared to the traditional one-pion exchange approximation (167).

5. Summary and outlook

In this article, we have reviewed recent progress in ChEFT calculations of nuclear matter properties (with quantified uncertainties) and their implications in the field of nuclear astrophysics. Combined with observational and experimental constraints, these microscopic calculations provide the basis for improved modeling of supernovae, neutron stars, and neutron star mergers. In particular, we have highlighted MBPT as an efficient framework for studying the nuclear EOS and transport properties across a wide range of densities, isospin asymmetries, and temperatures. We have also shown how advances in high-performance computing have enabled the implementation of two- and multi-nucleon forces in MBPT up to high orders in the chiral and many-body expansions. Finally, we have described new tools for quantifying theoretical uncertainties (especially EFT truncation errors) to confront microscopic calculations of the nuclear EOS with empirical constraints. Such systematic studies are particularly important in view of EOS constraints anticipated in the new era of multimessenger astronomy; *e.g.*, from gravitational wave detection, mass-radius measurements of neutron stars, and experiments with neutron-rich nuclei.

In the following we briefly summarize several open research directions at the interface of nuclear EFT and high-energy nuclear astrophysics. (i) EFT truncation errors and their correlations in density and across observables need to be studied with different many-body frameworks and nuclear interactions at arbitrary isospin asymmetry and finite temperature. (ii) Together with EFT truncation errors, the uncertainties in the LECs parametrizing the

interactions need to be quantified and propagated to nuclear matter properties using a comprehensive Bayesian statistical analysis. (iii) The full uncertainty quantification of the nuclear EOS will be aided by the development of improved order-by-order chiral NN and 3N potentials and the study of different regularization schemes as well as delta-full chiral interactions. (iv) Many-body calculations of nuclear matter properties beyond the nuclear EOS (*e.g.*, linear response and transport coefficients) with chiral NN and 3N interactions are required for more accurate numerical simulations of supernovae and neutron star mergers. (v) Future neutron star observations will provide stringent tests of nuclear forces and nuclear many-body methods in a regime that is presently largely unconstrained. The interplay between observation, experiment, and theory in the next decade can be expected to result in many further advances in our understanding of strongly interacting matter.

DISCLOSURE STATEMENT

The authors are not aware of any affiliations, memberships, funding, or financial holdings that might be perceived as affecting the objectivity of this review.

ACKNOWLEDGMENTS

We are very grateful to our collaborators and colleagues for fruitful discussions over the years that contributed in one way or another to the completion of this review article. We specifically thank Evgeny Epelbaum for providing us with the diagrams in Figure 1 and Yeunhwan Lim for sharing the results of Figures 7 and 8. C.D. acknowledges support by the Alexander von Humboldt Foundation through a Feodor-Lynen Fellowship and thanks the N3AS and BUQEYE Collaborations for creating warm research environments. This material is based upon work supported by the U.S. Department of Energy, Office of Science, Office of Nuclear Physics, under the FRIB Theory Alliance award DE-SC0013617. The work of J.W.H. was supported by the National Science Foundation under Grant No. PHY1652199 and by the U.S. Department of Energy National Nuclear Security Administration under Grant No. DE-NA0003841. C.W. has been supported by the Deutsche Forschungsgemeinschaft (DFG, German Research Foundation) – Project-ID 279384907 – SFB 1245.

LITERATURE CITED

1. Özel F, Freire P. *Annu. Rev. Astron. Astrophys.* 54:401 (2016)
2. Watts AL, et al. *Rev. Mod. Phys.* 88:021001 (2016)
3. Baiotti L. *Prog. Part. Nucl. Phys.* 109:103714 (2019)
4. Hergert H. *Front. in Phys.* 8:379 (2020)
5. Stroberg SR, Bogner SK, Hergert H, Holt JD. *Ann. Rev. Nucl. Part. Sci.* 69:307 (2019)
6. Lynn J, Tews I, Gandolfi S, Lovato A. *Ann. Rev. Nucl. Part. Sci.* 69:279 (2019)
7. Hebeler K, Holt J, Menendez J, Schwenk A. *Ann. Rev. Nucl. Part. Sci.* 65:457 (2015)
8. Epelbaum E, Hammer HW, Meißner UG. *Rev. Mod. Phys.* 81:1773 (2009)
9. Machleidt R, Entem DR. *Phys. Rep.* 503:1 (2011)
10. Hammer HW, König S, van Kolck U. *Rev. Mod. Phys.* 92:025004 (2020)
11. Hammer HW, Nogga A, Schwenk A. *Rev. Mod. Phys.* 85:197 (2013)
12. Epelbaum E, Krebs H, Reinert P. *Front. in Phys.* 8:98 (2020)
13. Furnstahl R, Klco N, Phillips D, Wesolowski S. *Phys. Rev. C* 92:024005 (2015)
14. Weinberg S. *Phys. Lett. B* 251:288 (1990)

15. Weinberg S. *Nucl. Phys. B* 363:3 (1991)
16. Weinberg S. *Phys. Lett. B* 295:114 (1992)
17. Reinert P, Krebs H, Epelbaum E. *Eur. Phys. J. A* 54:86 (2018)
18. Jiang W, et al. *Phys. Rev. C* 102:054301 (2020)
19. Piarulli M, Tews I. *Front. in Phys.* 7:245 (2020)
20. Hoferichter M, Ruiz de Elvira J, Kubis B, Meißner UG. *Phys. Rev. Lett.* 115:192301 (2015)
21. Hoppe J, et al. *Phys. Rev. C* 96:054002 (2017)
22. Bogner S, Kuo T, Coraggio L. *Nucl. Phys. A* 684:432 (2001)
23. Bogner S, Furnstahl R, Schwenk A. *Prog. Part. Nucl. Phys.* 65:94 (2010)
24. Hebeler K, Furnstahl RJ. *Phys. Rev. C* 87:031302 (2013)
25. Keller J, Wellenhofer C, Hebeler K, Schwenk A. *Phys. Rev. C* 103:055806 (2021)
26. Hebeler K, et al. *Phys. Rev. C* 83:031301 (2011)
27. Drischler C, Hebeler K, Schwenk A. *Phys. Rev. Lett.* 122:042501 (2019)
28. Simonis J, et al. *Phys. Rev. C* 96:014303 (2017)
29. Stroberg S, Holt J, Schwenk A, Simonis J. *Phys. Rev. Lett.* 126:022501 (2021)
30. Hüther T, et al. *Phys. Lett. B* 808:135651 (2020)
31. Weinberg S. *Phys. Rev.* 131:440 (1963)
32. Szabo A, Ostlund NS. New York: Dover Publications (1982), *Modern Quantum Chemistry: Introduction to Advanced Electronic Structure Theory*
33. Mariño M, Reis T. *J. Stat. Mech.* 2019:123102 (2019)
34. Arthuis P, et al. *Comp. Phys. Comm.* 240:202 (2019)
35. Day BD. *Rev. Mod. Phys.* 39:719 (1967)
36. Wellenhofer C. *Phys. Rev. C* 99:065811 (2019)
37. Kohn W, Luttinger JM. *Phys. Rev.* 118:41 (1960)
38. Wellenhofer C, Holt JW, Kaiser N, Weise W. *Phys. Rev. C* 89:064009 (2014)
39. Holt JW, Kaiser N. *Phys. Rev. C* 95:034326 (2017)
40. Hagen G, Papenbrock T, Hjorth-Jensen M, Dean DJ. *Rep. Prog. Phys* 77:096302 (2014)
41. Lu BN, et al. *Phys. Rev. Lett.* 125:192502 (2020)
42. Dickhoff WH, Barbieri C. *Prog. Part. Nucl. Phys.* 52:377 (2004)
43. Rios A. *Front. in Phys.* 8:387 (2020)
44. Carbone A, Rios A, Polls A. *Phys. Rev. C* 90:054322 (2014)
45. Carbone A, Polls A, Rios A. *Phys. Rev. C* 98:025804 (2018)
46. Drischler C, Carbone A, Hebeler K, Schwenk A. *Phys. Rev. C* 94:054307 (2016)
47. Tews I, Gandolfi S, Gezerlis A, Schwenk A. *Phys. Rev. C* 93:024305 (2016)
48. Lynn J, et al. *Phys. Rev. Lett.* 116:062501 (2016)
49. Lonardonì D, Tews I, Gandolfi S, Carlson J. *Phys. Rev. Res.* 2:022033 (2020)
50. Hebeler K, et al. *Phys. Rev. C* 91:044001 (2015)
51. Hebeler K. *Phys. Rept.* 890:1 (2021)
52. Holt JW, Kawaguchi M, Kaiser N. *Front. Phys.* 8:100 (2020)
53. Holt JW, Kaiser N, Weise W. *Phys. Rev. C* 79:054331 (2009)
54. Hebeler K, Schwenk A. *Phys. Rev. C* 82:014314 (2010)
55. Wellenhofer C, Holt JW, Kaiser N. *Phys. Rev. C* 92:015801 (2015)
56. Drischler C, Hebeler K, Schwenk A. *Phys. Rev. C* 93:054314 (2016)
57. Kaiser N arXiv:2010.02739 (2020)
58. Hagen G, et al. *Phys. Rev. C* 89:014319 (2014)
59. Kaiser N. *Eur. Phys. J. A* 48:58 (2012)
60. Dyhdalo A, Furnstahl R, Hebeler K, Tews I. *Phys. Rev. C* 94:034001 (2016)
61. Dyhdalo A, Bogner S, Furnstahl R. *Phys. Rev. C* 96:054005 (2017)
62. Carlsson BD, et al. *Phys. Rev. X* 6:011019 (2016)
63. Sammarruca F, et al. *Phys. Rev. C* 91:054311 (2015)
64. Drischler C, Melendez J, Furnstahl R, Phillips D. *Phys. Rev. C* 102:054315 (2020)

65. Rentmeester MCM, Timmermans RGE, de Swart JJ. *Phys. Rev. C* 67:044001 (2003)
66. Coraggio L, et al. *Phys. Rev. C* 87:014322 (2013)
67. Huth S, Wellenhofer C, Schwenk A. *Phys. Rev. C* 103:025803 (2021)
68. Drischler C, Somà V, Schwenk A. *Phys. Rev. C* 89:025806 (2014)
69. Wellenhofer C, Holt JW, Kaiser N. *Phys. Rev. C* 93:055802 (2016)
70. Roca-Maza X, Paar N. *Prog. Part. Nucl. Phys.* 101:96 (2018)
71. Drischler C, Krüger T, Hebeler K, Schwenk A. *Phys. Rev. C* 95:024302 (2017)
72. Furnstahl R, Phillips D, Wesolowski S. *J. Phys. G* 42:034028 (2015)
73. Melendez J, et al. *Phys. Rev. C* 100:044001 (2019)
74. Epelbaum E, Krebs H, Meißner U. *Eur. Phys. J. A* 51:53 (2015)
75. Drischler C, Furnstahl R, Melendez J, Phillips D. *Phys. Rev. Lett.* 125:202702 (2020)
76. Melendez J, Wesolowski S, Furnstahl R. *Phys. Rev. C* 96:024003 (2017)
77. Leonhardt M, et al. *Phys. Rev. Lett.* 125:142502 (2020)
78. Tews I, Krüger T, Hebeler K, Schwenk A. *Phys. Rev. Lett.* 110:032504 (2013)
79. Hoppe J, et al. *Phys. Rev. C* 100:024318 (2019)
80. Akmal A, Pandharipande VR, Ravenhall DG. *Phys. Rev. C* 58:1804 (1998)
81. Baldo M, Bombaci I, Burgio GF. *Astron. Astrophys.* 328:274 (1997)
82. Mütter H, Prakash M, Ainsworth TL. *Phys. Lett. B* 199:469 (1987)
83. Lim Y, Holt JW. *Phys. Rev. Lett.* 121:062701 (2018)
84. Tews I, Lattimer JM, Ohnishi A, Kolomeitsev EE. *Astrophys. J.* 848:105 (2017)
85. Tsang MB, et al. *Phys. Rev. Lett.* 102:122701 (2009)
86. Chen LW, Ko CM, Li BA, Xu J. *Phys. Rev. C* 82:024321 (2010)
87. Trippa L, Colo G, Vigezzi E. *Phys. Rev. C* 77:061304(R) (2008)
88. Tamii A, et al. *Phys. Rev. Lett.* 107:062502 (2011)
89. Roca-Maza X, et al. *Phys. Rev. C* 88:024316 (2013)
90. Kortelainen M, Lesinski T, et al. *Phys. Rev. C* 82:024313 (2010)
91. Danielewicz P, Singh P, Lee J. *Nucl. Phys. A* 958:147 (2017)
92. Hebeler K, Lattimer J, Pethick C, Schwenk A. *Phys. Rev. Lett.* 105:161102 (2010)
93. Gandolfi S, Carlson J, Reddy S. *Phys. Rev. C* 85:032801 (2012)
94. Horowitz C, et al. *J. Phys. G* 41:093001 (2014)
95. Essick R, et al. *Phys. Rev. C* 102:055803 (2020)
96. Cai BJ, Chen LW. *Phys. Rev. C* 85:024302 (2012)
97. Steiner AW. *Phys. Rev. C* 74:045808 (2006)
98. Somasundaram R, Drischler C, Tews I, Margueron J. *Phys. Rev. C* 103:045803 (2021)
99. Kaiser N. *Phys. Rev. C* 91:065201 (2015)
100. Wen P, Holt JW arXiv:2012.02163 (2020)
101. Elliott JB, Lake PT, Moretto LG, Phair L. *Phys. Rev. C* 87:054622 (2013)
102. Fore B, Reddy S. *Phys. Rev. C* 101:035809 (2020)
103. Petschauer S, et al. *Front. in Phys.* 8:12 (2020)
104. Holt JW, Kaiser N, Weise W. *Prog. Part. Nucl. Phys.* 73:35 (2013)
105. Holt JW, Rho M, Weise W. *Phys. Rept.* 621:2 (2016)
106. Schneider AS, Horowitz CJ, Hughto J, Berry DK. *Phys. Rev. C* 88:065807 (2013)
107. Karnaukhov VA, et al. *Phys. Atom. Nucl.* 71:2067 (2008)
108. Beegle BL, Modell M, Reid RC. *Amer. Inst. Chem. Eng. J.* 20:1200 (1974)
109. Ducoin C, Chomaz P, Gulminelli F. *Nucl. Phys. A* 771:68 (2006)
110. Carbone A, Schwenk A. *Phys. Rev. C* 100:025805 (2019)
111. Yasin H, Schäfer S, Arcones A, Schwenk A. *Phys. Rev. Lett.* 124:092701 (2020)
112. Bauswein A, Janka HT, Oechslin R. *Phys. Rev. D* 82:084043 (2010)
113. Oertel M, Hempel M, Klähn T, Typel S. *Rev. Mod. Phys.* 89:015007 (2017)
114. Lattimer JM, Prakash M. *Astrophys. J.* 550:426 (2001)
115. Tsang C, et al. *Phys. Lett. B* 796:1 (2019)

116. Özel F, et al. *Astrophys. J.* 820:28 (2016)
117. Nättilä J, et al. *Astron. Astrophys.* 608:A31 (2017)
118. Miller MC, et al. *Astrophys. J.* 887:L24 (2019)
119. Riley TE, et al. *Astrophys. J.* 887:L21 (2019)
120. Annala E, et al. *Nature Phys.* 16:907 (2020)
121. Baym G, Pethick C, Sutherland P. *Astrophys. J.* 170:299 (1971)
122. Greif S, et al. *Mon. Not. Roy. Astron. Soc.* 485:5363 (2019)
123. Tews I, Margueron J, Reddy S. *Eur. Phys. J. A* 55:97 (2019)
124. Lim Y, Holt J. *Eur. Phys. J. A* 55:209 (2019)
125. Tews I, Carlson J, Gandolfi S, Reddy S. *Astrophys. J.* 860:149 (2018)
126. Lyne AG, et al. *Science* 303:1153 (2004)
127. Lattimer JM, Schutz BF. *Astrophys. J.* 629:979 (2005)
128. Hu H, et al. *Mon. Not. Roy. Astr. Soc.* 497:3118 (2020)
129. Lim Y, Holt JW, Stahulak R.J. *Phys. Rev. C* 100:035802 (2019)
130. Greif S, et al. *Astrophys. J.* 901:155 (2020)
131. Raithel CA, Özel F, Psaltis D. *Phys. Rev. C* 93:032801 (2016)
132. Demorest PB, et al. *Nature* 467:1081 (2010)
133. Antoniadis J, et al. *Science* 340:6131 (2013)
134. Cromartie HT, et al. *Nature Astronomy* 4:72 (2019)
135. Alford MG, Han S, Prakash M. *Phys. Rev. D* 88:083013 (2013)
136. Drischler C, et al. *Phys. Rev. C* 103:045808 (2021)
137. Flanagan EE, Hinderer T. *Phys. Rev. D* 77:021502 (2008)
138. Annala E, Gorda T, Kurkela A, Vuorinen A. *Phys. Rev. Lett.* 120:172703 (2018)
139. Yagi K, Yunes N. *Phys. Rev. D* 88:023009 (2013)
140. Bauswein A, Janka HT, Hebeler K, Schwenk A. *Phys. Rev. D* 86:063001 (2012)
141. Bauswein A, et al. *Phys. Rev. Lett.* 122:061102 (2019)
142. Abbott BP, et al. *Phys. Rev. Lett.* 119:161101 (2017)
143. Abbott BP, et al. *Astrophys. J. Lett.* 848:L12 (2017)
144. Abbott BP, et al. *Phys. Rev. Lett.* 121:161101 (2018)
145. Tews I, Margueron J, Reddy S. *Phys. Rev. C* 98:045804 (2018)
146. Abbott BP, et al. *Phys. Rev. X* 9:011001 (2019)
147. Fattoyev FJ, Piekarewicz J, Horowitz CJ. *Phys. Rev. Lett.* 120:172702 (2018)
148. Metzger BD, et al. *Mon. Not. Roy. Astr. Soc.* 406:2650 (2010)
149. Bauswein A, Just O, Janka HT, Stergioulas N. *Astrophys. J. Lett.* 850:L34 (2017)
150. Margalit B, Metzger BD. *Astrophys. J. Lett.* 850:L19 (2017)
151. Shibata M, et al. *Phys. Rev. D* 96:123012 (2017)
152. Radice D, Perego A, Zappa F, Bernuzzi S. *Astrophys. J. Lett.* 852:L29 (2018)
153. Rezzolla L, Most ER, Weih LR. *Astrophys. J. Lett.* 852:L25 (2018)
154. Capano CD, et al. *Nature Astron.* 4:625 (2020)
155. Lim Y, Bhattacharya A, Holt JW, Pati D arXiv:2007.06526 (2020)
156. Raaijmakers G, et al. *Astrophys. J. Lett.* 893:L21 (2020)
157. Janka HT, et al. *Phys. Rept.* 442:38 (2007)
158. Pons JA, et al. *Astrophys. J.* 513:780 (1999)
159. Roberts LF, Woosley SE, Hoffman RD. *Astrophys. J.* 722:954 (2010)
160. Müller B. *Publ. Astron. Soc. Aust.* 33:e048 (2016)
161. Schneider AS, Roberts LF, Ott CD, O'Connor E. *Phys. Rev. C* 100:055802 (2019)
162. Rrapaj E, Roggero A, Holt JW. *Phys. Rev. C* 93:065801 (2016)
163. Du X, Steiner AW, Holt JW. *Phys. Rev. C* 99:025803 (2019)
164. Roberts LF, Reddy S, Shen G. *Phys. Rev. C* 86:065803 (2012)
165. Martínez-Pinedo G, Fischer T, Lohs A, Huther L. *Phys. Rev. Lett.* 109:251104 (2012)
166. Rrapaj E, et al. *Phys. Rev. C* 91:035806 (2015)

167. Bartl A, Pethick C, Schwenk A. *Phys. Rev. Lett.* 113:081101 (2014)